ACS OMEGA

Open Access

http://pubs.acs.org/journal/acsodf

Article

Doping-Induced Relaxor Ferroelectricity and Site Engineering in $Ba_{1-x}Pr_{2x/3}Ti_{1-y}(Mo_{1/2}Nb_{1/2})_yO_3$ Ceramics for Enhanced Permittivity and Energy Storage Performance

Published as part of ACS Omega special issue "Energy Storage across Scales".

Deep Mala, Chandra Bhal Singh, and Akhilesh Kumar Singh*

Cite This: *ACS Omega* 2025, 10, 43779−43796

Read Online

ACCESS | Metrics & More | Article Recommendations

ABSTRACT: In this study, site engineering at the Ba and Ti sites of $BaTiO_3$ has been done to develop $Ba_{1-x}Pr_{2x/3}Ti_{1-y}(Mo_{1/2}Nb_{1/2})_yO_3$ [BTMN] ceramics, with x = 0.003 and y = 0.02, 0.04, 0.06, 0.08, 0.1, to improve permittivity and energy storage performance. The solid-state reaction method was used to synthesize samples. X-ray diffraction analysis revealed a crystallographic phase transition from tetragonal ($P4mm$) to cubic ($Pm\text{-}3m$) structure with increasing $(Mo_{1/2}Nb_{1/2})$ concentration. Raman spectroscopy further validates this finding with the disappearance of the characteristic tetragonal peak at 303 cm^{-1} for higher dopant levels ($y \geq 0.06$). Grain size displays a nonlinear trend where grain size first increases to 0.49 μm for intermediate compositions and then decreases to 0.25 μm at higher dopant levels. Dielectric characterization revealed that the increased relative permittivity (ε_r = 2840.46 at 20 Hz) and low dielectric loss (0.0390) have been achieved for the BTMN06 sample, and all other compositions exhibited low dielectric loss (<0.055) in the frequency range 20 Hz to 100 kHz. Permittivity decreased with increasing frequency, which is consistent with Maxwell−Wagner polarization effects. Curie temperature (T_c) shifted downward from 115 °C (BTMN02) to 31 °C (BTMN10), reflecting increased structural disorder induced by doping. Relaxor behavior was quantified by an increasing diffusion parameter (1.28 to 1.95) for permittivity, with enhanced polarization stability and slim P−E hysteresis loops at higher dopant levels. Energy storage characteristics showed superior recoverable energy densities (317.7 mJ/cm^3 for BTMN08 and 292.2 mJ/cm^3 for BTMN10 with efficiencies 91 and 92.6% respectively), validating the material's potential for high-efficiency capacitive energy storage in advanced applications.

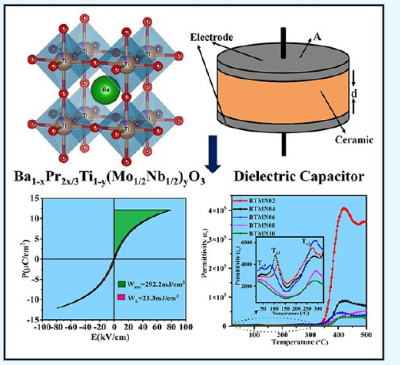

1. INTRODUCTION

As energy consumption surges, there is a growing need across the globe to develop renewable energy sources that are both affordable and environmentally conscious. A key element in realizing a smart and sustainable energy solution is high-performance energy storage systems.[1] Currently, the primary energy storage technologies include batteries, dielectric capacitors, electrochemical capacitors, and fuel cells. Dielectric capacitors have emerged as crucial elements in pulse power systems because of their extremely fast charge and discharge rates along with their exceptionally high-power density.[1,2] Different types of energy storage materials have been synthesized for dielectric capacitors, which include both organic and inorganic types like ceramics, polymers, composites of ceramics−polymers, glass, and glass−ceramic composites. Dielectric ceramics, in comparison to other materials, have a moderate breakdown field strength, low dielectric loss, and fatigue-resistant properties and are regarded as the ideal materials for high-temperature uses because of their outstanding temperature stability. These characteristics of dielectric ceramics present significant opportunities for the application of energy storage capacitors in aerospace, oil extraction, electromagnetic pulse weapons, integrated circuits, electric vehicles, and several other fields.[3] Dielectric ceramics based on their polarization and dielectric permittivity are classified into linear dielectric (LD), ferroelectric (FE), antiferroelectric (AFE), and relaxor ferroelectric (RFE).[4] In dielectric capacitors, a ceramic placed between two electrodes polarizes under an electric field storing energy with capacitance $C = \varepsilon_0\varepsilon_r A/d$, where ε_0 is the permittivity of free space, ε_r is the relative permittivity (dielectric constant), A is the area, and d is the thickness of the parallel plate capacitor shown in Figure 1a,b.[5] The energy storage density in the case of linear dielectric

Received: May 6, 2025
Revised: July 26, 2025
Accepted: September 9, 2025
Published: September 18, 2025

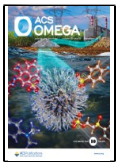

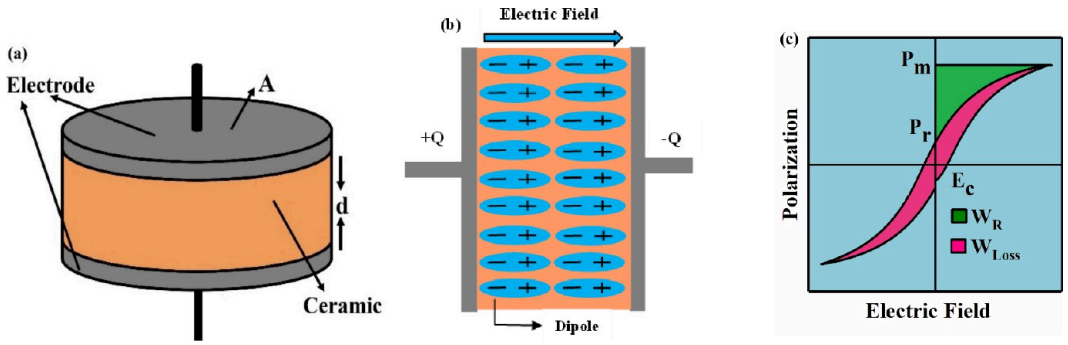

Figure 1. (a) Schematic representation of a parallel plate capacitor with thickness d and area A. (b) Mechanism of the dielectric capacitor with dipoles oriented with electric field. (c) Polarization versus electric field loop with energy storage parameters.

capacitors is given as $W = \frac{1}{2}\varepsilon_0\varepsilon_r E^2$, where E is the applied electric field, whereas in the case of nonlinear dielectric (FE, AFE, and RFE) capacitors, polarization displays a hysteresis effect with the electric field leading to energy loss; hence, total energy density (W_T), recoverable energy density (W_R), energy loss (W_{Loss}), and efficiency (η) are given as

$$W_T = \int_0^{P_m} E\,dP \tag{1}$$

$$W_R = \int_{P_r}^{P_m} E\,dP \tag{2}$$

$$W_{Loss} = W_T - W_R \tag{3}$$

$$\eta = \frac{W_R}{W_T} \times 100 \tag{4}$$

where P is the polarization, P_m is the maximum polarization, P_r is the remnant polarization, and E is the electric field, as shown in Figure 1c.[6,7]

In normal ferroelectrics, the dielectric behavior follows the Curie–Weiss law above the Curie temperature, expressed as $\frac{1}{\varepsilon} = \frac{T - T_0}{C}$, where ε is the dielectric permittivity, T_0 is the Curie–Weiss temperature, C is the Curie–Weiss constant. Relaxor ferroelectrics show a deviation from this law and follow the modified Curie–Weiss expression:

$$\frac{1}{\varepsilon} - \frac{1}{\varepsilon_m} = \frac{(T - T_m)^\gamma}{C} \tag{5}$$

where ε_m is the maximum value of dielectric permittivity, T_m is the temperature of maximum value of ε_m, C is the constant, and γ is the diffuseness parameter. This parameter ranges from 1 to 2; it is 1 for conventional ferroelectrics, between 1 and 2 for relaxors, and 2 for a fully diffuse phase transition.[8−10] Relaxor ferroelectrics can be distinguished from conventional ferroelectrics by three key characteristics: (i) a diffuse temperature-dependent response in the relative permittivity, (ii) the frequency-dependent dispersion of the permittivity maximum, and (iii) lack of macroscopic symmetry breaking across the temperature range of permittivity maximum. Therefore, the temperature at which the permittivity reaches its maximum is referred to as T_m rather than the Curie temperature T_c.[4,11] The temperature-dependent dielectric response plays a key role in probing the behavior of polar nanoregions (PNRs). The dielectric behavior of a typical relaxor ferroelectric (RFE) is governed by three distinct temperatures: T_f (freezing temperature), T_m (temperature of maximum permittivity), and T_B (Burns temperature), as illustrated in Figure 2. These three temperatures divide the

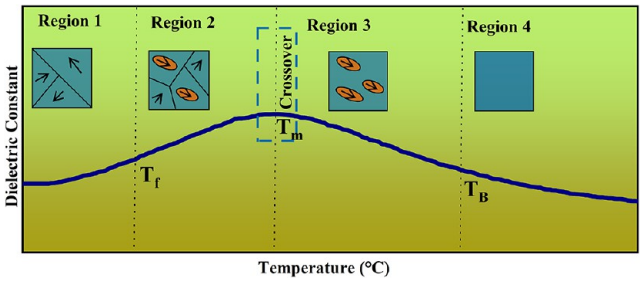

Figure 2. Schematic diagram of temperature-dependent dielectric permittivity along with their domain structure and characteristics temperature.

dielectric temperature spectrum into four distinct regions each exhibiting unique dielectric characteristics. In region 1, $T < T_f$, the dynamic polar nanoregions get frozen and the relaxor may undergo transition into a ferroelectric state characterized by the formation of ferroelectric macro-domains. Application of the electric field then results in strong ferroelectric hysteresis due to domain reorientation. In region 2, $T_f < T < T_m$, the relaxor state exists as a partially disordered state with a disrupted long-range ferroelectric order. Both nanodomains and microdomains coexist, leading to reduced ferroelectric hysteresis, and the dielectric properties exhibit significant frequency-dependent dispersion. In region 3, above T_m ($T > T_m$), spontaneous polarization disappears in some regions of the relaxor leading to the complete breakdown of micro-domains. The material predominantly consists of highly dynamic polar nanodomains with minimal ferroelectric hysteresis. In region 4, beyond T_B ($T > T_B$), polar regions disappear, and the relaxor completely transitions into a paraelectric state. The polar characteristics are fully suppressed in this region.[12−14]

$BaTiO_3$-based perovskite oxides known for their ferroelectric and relaxor ferroelectric properties possess significant technological potential in energy storage applications.[15] Modifying the intrinsic properties of $BaTiO_3$ via incorporation of dopants at either the A site (Ba^{2+}) or B site (Ti^{4+}) of the perovskite structure induces a transition from normal ferroelectric behavior to a diffuse phase transition (DPT) and eventually to relaxor ferroelectric at higher levels of substitution. Merselmiz et al. studied $BaTi_{0.89}Sn_{0.11}O_3$ (BTSn) ceramics, which show a high dielectric constant of 17,390 at 41 °C and a

https://doi.org/10.1021/acsomega.5c04164
ACS Omega 2025, 10, 43779−43796

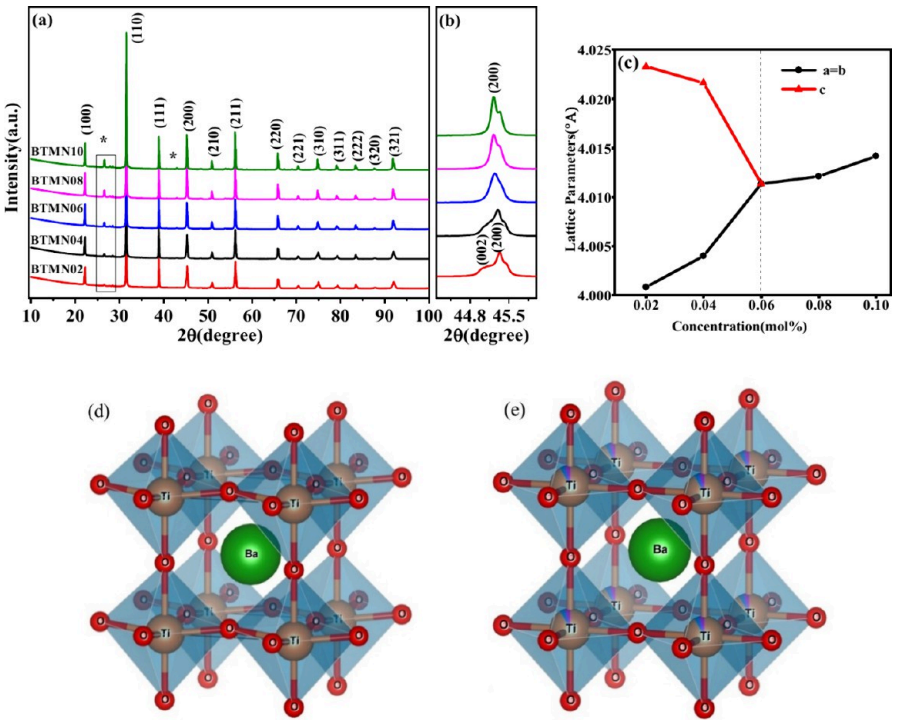

Figure 3. (a) Room-temperature XRD pattern of $Ba_{1-x}Pr_{2x/3}Ti_{1-y}(Mo_{1/2}Nb_{1/2})_yO_3$ with x = 0.003 and y = 0.02, 0.04, 0.06, 0.08, 0.10. Bragg diffraction indices of the cubic structure marked. (b) Enlarged view of the (200) peak showing tetragonal splitting at lower concentrations of doping. (c) Variation of lattice parameters with composition. (d, e) Polyhedral crystal structure of BTMN02 and BTMN10, showing tetragonal and cubic structures, respectively, drawn from VESTA software using results of the Rietveld refinement.

recovered energy density of 84.4 mJ/cm^3 with 91.04% energy efficiency at 60 °C, and it is increasing to 95.87% at 100 °C.[16] Khardazi et al. studied $Ba_{1-x}La_xTi_{0.89}Sn_{0.11}O_3$ (x = 0−0.035), which shows enhanced values in the BLTSn2.5 sample with 158.8 mJ/cm^3 and 82.73% at room temperature and dielectric constants between 620 and 725 (100 Hz−1 MHz).[17] Ma et al. studied the $(1-x)BaTiO_3$-$xBi(Y_{1/3}Ti_{1/2})O_3$ system, which yielded a recoverable energy storage of 1.02 J/cm^3 and an efficiency of 78% when x = 0.15 and gave 0.77 J/cm^3 and 90% when x = 0.2, and a dielectric constant of 2573 is reported for x = 0.2.[18] Liu et al. studied the 0.8 $Bi_{0.5}Na_{0.5}TiO_3$-0.2$NaNbO_3$ system, and a high W_{rec} of ∼7.22 J/cm^3 and an efficiency of ∼95.32% were achieved under 515 kV/cm with dielectric constant <1000.[19] Balmuchu et al. studied $(1-x)BaTiO_3$-$xBi[Zn_{2/3}(Nb_{0.85}Ta_{0.15})_{1/3}]O_3$, x = 0.05−0.25 and reported W_{rec} = 2.06 J/cm^3 and 78% efficiency for x = 0.15 with η improving to 96% at higher substitution under 180 kV/cm.[20] Adediji et al. compared the energy storage performance of various $BaTiO_3$-based compositions in terms of energy density, efficiency, and film thickness. For 0.84BT-0.16BNZ (150 μm), the energy density and efficiency were 2.485 J/cm^3 and 96.02%, respectively. The 0.88BST-0.12BZN composition (130 μm) exhibited an energy density of 1.62 J/cm^3 and an efficiency of 99.8%, while 0.9BST-0.1BMN (200 μm) showed an energy density of 3.34 J/cm^3 with 85.71% efficiency. In 0.95BT−0.05BN (300 μm), the energy density is 0.68 J/cm^3 and the efficiency is 91.5%.[21] On comparison of energy storage and efficiency with thickness, $Ba_{1-x}Pr_{2x/3}Ti_{1-y}(Mo_{1/2}Nb_{1/2})_yO_3$ has better energy storage and efficiency.

In this study, $Ba_{1-x}Pr_{2x/3}Ti_{1-y}(Mo_{1/2}Nb_{1/2})_yO_3$, x = 0.03, y = 0.02, 0.04, 0.06, 0.08, 0.1, ceramics have been synthesized and characterized for energy storage applications by a site engineering method. Pr is substituted at the A site, while Mo and Nb are substituted as B-site dopants, in the $BaTiO_3$ lattice with the A-site dopant concentration held constant and varying B-site dopant concentrations. This doping aims to disrupt the long-range ferroelectric order, facilitating the formation of polar nanodomains that enhances the materials relaxor behavior.

The majority of earlier research either maintains fixed stoichiometric ratios between A- and B-site dopants or concentrates on single-site doping. This study establishes precise structure−property relationships, identifies synergistic effects between fixed A-site and variable B-site doping, and decouples the individual contributions of A- and B-site dopants by varying B-site (Mo, Nb) doping while maintaining a constant A-site (Pr) concentration. This strategy fills in a number of significant gaps in the literature on site-specific doping effects in perovskite materials, while building on an extensive amount of prior research.

2. EXPERIMENTAL DETAILS

2.1. Synthesis of Materials. $Ba_{1-x}Pr_{2x/3}Ti_{1-y}(Mo_{1/2}Nb_{1/2})_yO_3$, where x = 0.003 and y = 0.02, 0.04, 0.06, 0.08, 0.1 abbreviated as BTMN02 (y = 0.02), BTMN04 (y = 0.04), BTMN06 (y = 0.06), BTMN08 (y = 0.08), and BTMN10 (y = 0.1) were synthesized by the solid-state reaction method. High-purity reactant powders of $BaCO_3$ (Sigma-Aldrich, 99%), TiO_2 (Sigma-Aldrich grade, 99%), Nb_2O_5 (Sigma-Aldrich, 99%), Mo_2O_5 (Sigma-Aldrich, 99%), and Pr_6O_{11} (Analytical Reagent, 99.9%) were the starting materials for the synthesis. The precursor powders were stoichiometrically weighed and milled in a high-energy ball mill (Retsch PM 400 MA, Germany). The analytical reagent (AR)-grade ethanol medium and 5 mm zirconium balls were used for milling for 6 h at 300 rpm keeping the powder-to-ball ratio to

https://doi.org/10.1021/acsomega.5c04164
ACS Omega 2025, 10, 43779−43796

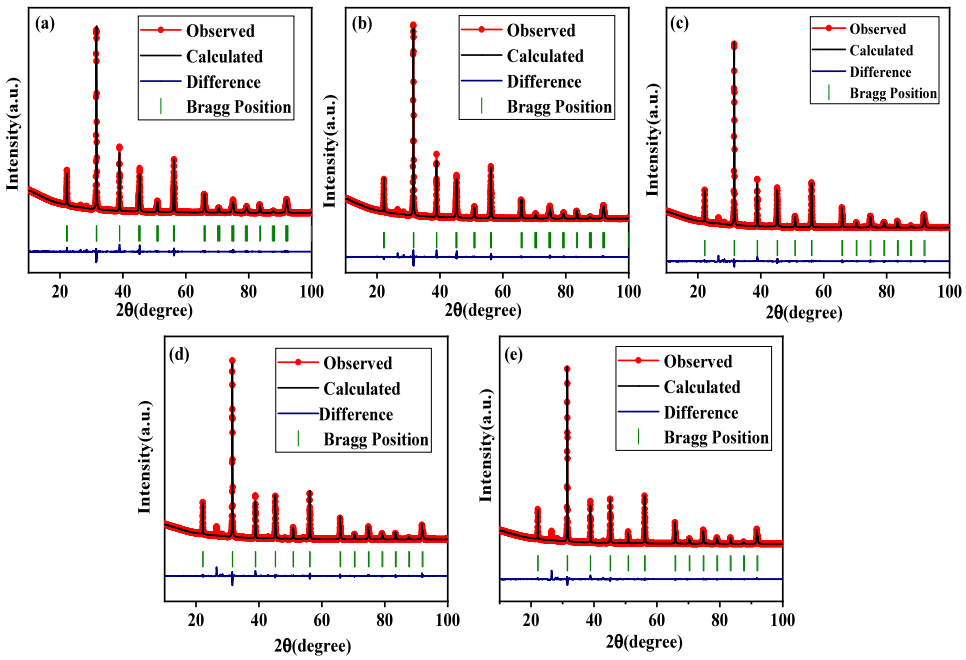

Figure 4. Rietveld fits of XRD patterns of $Ba_{1-x}Pr_{2x/3}Ti_{1-y}(Mo_{1/2}Nb_{1/2})_yO_3$ with (a) y = 0.02, (b) y = 0.04 for the tetragonal structure with the *P4mm* space group, and (c) y = 0.06, (d) y = 0.08, and (e) y = 0.10 for the cubic structure with the *Pm*-3m space group.

1:10. After milling, the wet material was first dried at 100 °C in a hot oven for evaporating ethanol and then ground in a mortar and pestle for 5 to 10 min. The obtained powder was calcined at 1200 °C for 6 h. In calcined powder, 5 wt % poly(vinyl alcohol) (PVA) solution in water was mixed as a binder and then pressed into pellets in a 10 mm steel die using a hydraulic press (Osho Scientific India) at a pressure of 10 tons. The binder burning was done at 500 °C for 5 h, followed by sintering of pellets at 1225 °C for 6 h.

2.2. Characterization. The crystal structure was examined by powder X-ray diffraction (XRD) of a Rigaku SmartLab diffractometer with Cu $K_{\alpha1}$ radiation of wavelength λ = 1.540593Å and Cu $K_{\alpha2}$ of wavelength λ = 1.544414 Å as well as XG current of 200 mA and XG voltage of 45 kV. Before recording the XRD pattern, the sintered pellet was crushed, ground, and annealed at 500 °C for 5 h. For structural analysis from the XRD data, Rietveld structure refinement using FullProf Suite was performed. Scanning electron microscopy (SEM) and elemental mapping were used to characterize the surface microstructure and elemental composition of the sample using Nova NanoSEM 450, FEI USA. Raman measurements were carried out at room temperature using a WITec alpha300 RAS model with a frequency range of 10 to 1000 cm^{-1}. X-ray photoelectron spectroscopy (XPS) spectra were collected using a Thermo Fisher Scientific XPS (K-alpha). The instrument was energy-calibrated using the reference metal Au $4f_7/_2$ peak at 84.96 eV, and the peak corresponding to the C 1s peak, which is located at 284.8 eV, was used as a reference for the binding energy scale throughout the experiment. The binding energy may carry an estimated uncertainty of ±0.2 eV. Analysis of the various XPS spectra was carried out by using XPSPEAK 4.1 software. UV−visible spectroscopy was done with a Jasco V-650 spectrometer to study the optical properties of the system. The ferroelectric hysteresis (P−E) loop and current electric field (J−E) response were recorded with a Radiant Precision Premier II ferroelectric tester. Temperature-dependent (30−500 °C) dielectric measurements in the frequency range of 20 kHz to 10 MHz were done using the Keysight E4990A Impedance Analyzer. For the above electrical measurement, the sintered pellets were silver coated on both flat sides to make electrodes.

3. RESULTS AND DISCUSSION

3.1. Structural Analysis. Figure 3a displays the room-temperature XRD patterns of the $Ba_{1-x}Pr_{2x/3}Ti_{1-y}(Mo_{1/2}Nb_{1/2})_yO_3$ samples for all the compositions, in the 2θ range of 10−100° with the step size of 0.02° at the scan rate of 3°/min. The characteristic splitting of the XRD peaks reveal that the sample with y = 0.02 and 0.04 exhibits a tetragonal structure with the *P4mm* space group. With increasing the concentration of Mo and Nb from y = 0.06 to 0.10, the structure transforms to cubic with the *Pm*-3*m* space group as all the XRD peaks appear as singlet. Figure 3b displays the enlarged XRD patterns of the peak in the 2θ range 44 to 46°, which shows that the splitting of (002) and (200) tetragonal peaks observed at low concentration merges to a single symmetric (200) peak for the cubic structure with increasing Mo/Nb concentration. A shoulder/peak on the right side of the (200) XRD profile is due to Cu $K_{\alpha2}$ radiation and not due to any structural origin. Few weak secondary phase peaks marked with asterisks (*) in the 2θ range of 26 to 29° and around 43° were also observed for the higher compositions, and they correspond to $BaMoO_4$ (#98-010-7406). It is also observed that the intensity as well as number of secondary peaks increases with increasing the concentration of Mo, signifying the decrease in solid solubility limit of the sample with increasing the dopant concentration.

Figure 4a−e shows the Rietveld Refinement fitting of the XRD patterns for various compositions. Rietveld structure refinement confirms the formation of a tetragonal structure with the *P4mm* space group for y = 0.02 and 0.04 and a cubic structure with the *Pm*-3*m* space group for y = 0.06, 0.08, and 0.10 compositions. The refined structural parameters are listed in Table 1. The composition-dependent variation of lattice

https://doi.org/10.1021/acsomega.5c04164
ACS Omega 2025, 10, 43779−43796

Table 1. Lattice Parameters and Unit Cell Volume of $Ba_{1-x}Pr_{2x/3}Ti_{1-y}(Mo_{1/2}Nb_{1/2})_yO_3$ Obtained after Rietveld Structure Refinement from the XRD Data

composition	structure	space group	lattice parameters (Å)	volume (Å^3)
BTMN02	tetragonal	*P*4*mm*	$a = b = 4.00084(4)$, $c = 4.02332(6)$	64.4003(12)
BTMN04	tetragonal	*P*4*mm*	$a = b = 4.000403(4)$, $c = 4.02165(6)$	64.4762(13)
BTMN06	cubic	*Pm*-3m	$a = b = c = 4.01133(3)$	64.5452(8)
BTMN08	cubic	*Pm*-3m	$a = b = c = 4.01209(3)$	64.5819(10)
BTMN10	cubic	*Pm*-3m	$a = b = c = 4.01419(3)$	64.6833(8)

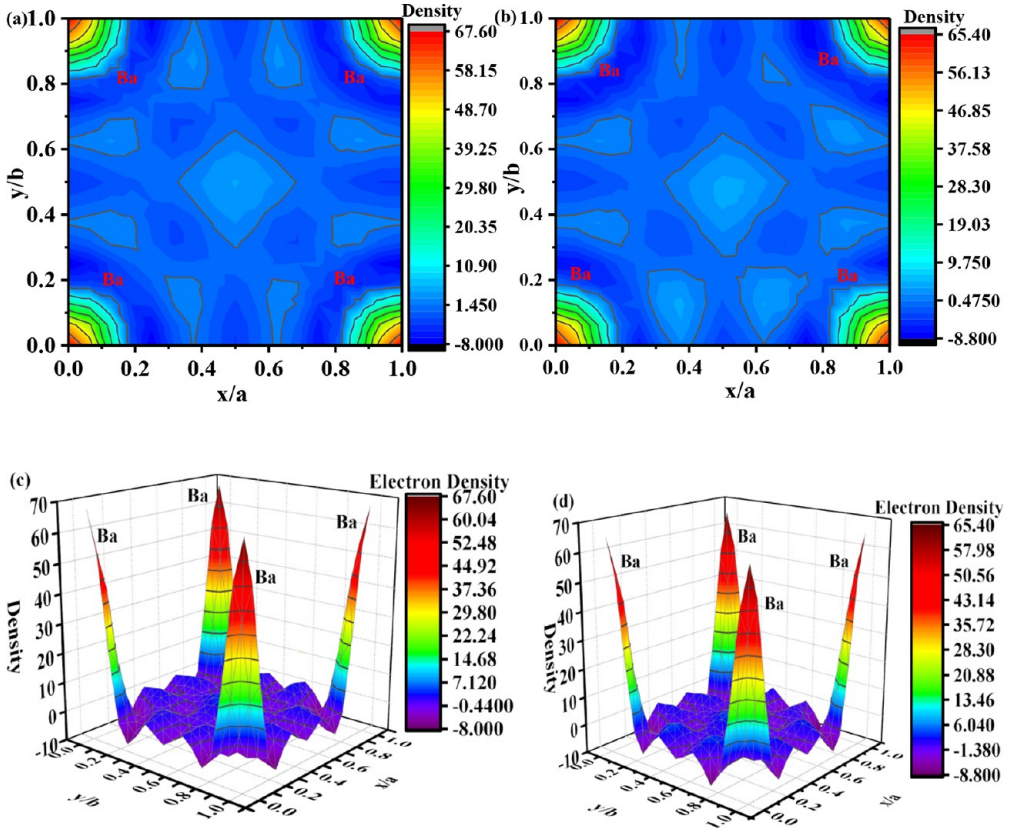

Figure 5. Two- and three-dimensional electron density mapping along x/a and y/b directions for BTMN02, $y = 0.02$ (a, c), and BTMN10, $y = 0.10$ (b, d).

parameters is shown in Figure 3c. It can be noted from Table 1 that as the concentration of dopant increases, the unit cell volume exhibits a corresponding increase. In nanocrystalline materials, the high surface energy contributes to lattice strain leading to lattice compression and a reduction in unit cell volume. For larger crystallites, the minimum surface energy reduces internal stress allowing the lattice to relax and expand. This relaxation leads to an increase in lattice parameters and the volume of the unit cell. On the basis of ionic size and coordination number of B−O_6 octahedra, an ionic size of 6 coordinated Ti^{4+} (0.60 Å) is comparable to Mo^{6+} (0.59 Å) and smaller compared to Nb^{5+} (0.64 Å), and the large difference in the ionic size of Nb compared to Mo and Ti causes lattice expansion and therefore increase in the lattice parameters and volume of the unit cell. Praseodymium (Pr) exists in multiple coordination states with different valences depending on the substitution site, 12 coordinated Pr^{3+} with ionic size 1.30 Å, 6 coordinated Pr^{3+} (B-site substitution) with size 0.99 Å, and 6 coordinated (B-site substitution) Pr^{4+} with size 0.85 Å. In perovskite-type ABO_3 compounds, Pr^{3+} (1.30 Å) is capable of substituting at the A site in a manner analogous to La^{3+} (1.36 Å) due to their similar ionic sizes. Hence, Pr is substituted in a very small amount at the Ba^{2+} (1.61 Å) site to cause distortions in the A-site lattice without disturbing the integrity of the BO_6 octahedra.[22]

The GFourier program in the FullProf suite was used to study the electron density distribution in different compositions of $Ba_{1-x}Pr_{2x/3}Ti_{1-y}(Mo_{1/2}Nb_{1/2})_yO_3$. The Rietveld structure refinement values were used to plot the electron density distribution mapping. The electron density is the Fourier transform of the structure factor obtained from the Rietveld refinement.[23] Figure 5a and Figure 5b represent the two-dimensional electron density mapping of $Ba_{1-x}Pr_{2x/3}Ti_{0.98}(Mo_{1/2}Nb_{1/2})_{0.02}O_3$ and $Ba_{1-x}Pr_{2x/3}Ti_{0.90}(Mo_{1/2}Nb_{1/2})_{0.10}O_3$ ($x = 0.003$) compositions, respectively, and Figure 5c,d represents the three-dimensional mapping of the same. The electron density is represented by the color contours. The high electron density area represents the elements with high atomic number.[24] The region from blue to red of the spectra indicates the increasing electron density regions. Ba ($Z = 56$)/Pr ($Z = 59$) at the A site has the high atomic number and therefore has maximum electron densities

https://doi.org/10.1021/acsomega.5c04164
ACS Omega 2025, 10, 43779−43796

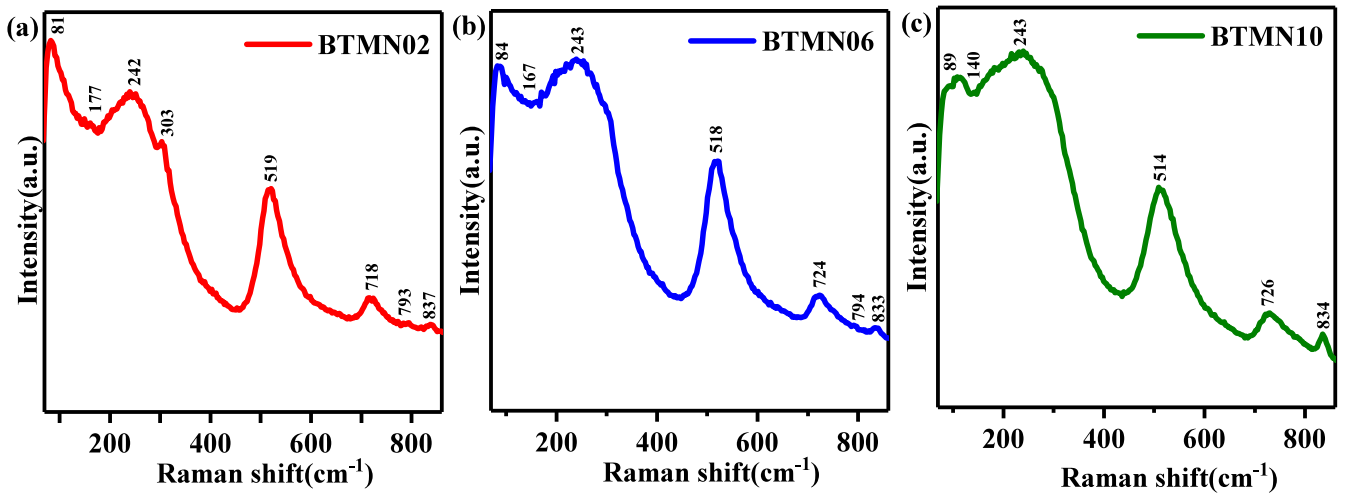

Figure 6. Room-temperature Raman spectra of $Ba_{1-x}Pr_{2x/3}Ti_{1-y}(Mo_{1/2}Nb_{1/2})_yO_3$ with x = 0.03 and (a) y = 0.02, (b) 0.06, and (c) 0.10.

of 67.60 and 65.40 e/Å^3 for BTMN02 and BTMN10, respectively.

3.2. Raman Spectroscopic Analysis. In order to get more light into the local symmetry of the crystal structure, phase transitions, defects, domain structure, and polarization (ferroelectric behavior), room-temperature Raman spectroscopy measurements were carried out. Figure 6 shows the Raman spectra of the samples with y = 0.02, 0.06, and 0.10, which coincides with the earlier reports.[22,25−29] The various modes of the spectra are as follows:

I. E(TO1) phonon mode, at 81 cm^{-1} (y = 0.02), 84 cm^{-1} (y = 0.06), 89 cm^{-1} (y = 0.10).
II. A dip assigned to A1(TO1), at 177 cm^{-1} (y = 0.02), 167 cm^{-1} (y = 0.06), 140 cm^{-1} (y = 0.10).
III. Broad peak A1(TO2) around 240 cm^{-1}.
IV. E1, B1(TO+LO) mode at 303 cm^{-1} (y = 0.02).
V. Asymmetry peak corresponds to A1(TO) and E(TO), at 519 cm^{-1} (y = 0.02), 518 cm^{-1} (y = 0.06), 514 cm^{-1} (y = 0.10).
VI. A1(LO) and E(LO), at 718 cm^{-1} (y = 0.02), 724 cm^{-1} (y = 0.06), 726 cm^{-1} (y = 0.10).
VII. i-LVM extra mode at 793 cm^{-1}.
VIII. ν-LVM extra mode, at 837 cm^{-1} (y = 0.02), 833 cm^{-1} (y = 0.06), 834 cm^{-1} (y = 0.10).

In the ideal cubic perovskite structure (defect free), Raman selection rules hold validity, and first-order Raman scattering is forbidden by symmetry. However, it does not hold good in the case of materials with chemical substitution, where even in the cubic phase well-defined Raman modes exist.[25] Here, the presence of Raman modes in the cubic phase samples is considered to be of first order that arises due to the structural disorder.[29−31] It is important here to note that the presence of ferroelectric microregions performing as symmetry-breaking defects also lead to the first-order Raman scattering in the cubic phase. In the perovskites $BaTiO_3$, the peak at 300 cm^{-1} is an indication of a tetragonal structure. In the $Ba_{1-x}Pr_{2x/3}Ti_{1-y}(Mo_{1/2}Nb_{1/2})_yO_3$ system, a small peak with a low intensity at 303 cm^{-1} for the composition with y = 0.02 confirms the tetragonal structure. With increasing concentration, for y = 0.06 and y = 0.10, this peak disappears indicating a phase transition from tetragonal to cubic structure, which is in agreement with the XRD results.[25] The localized vibrational modes (i-LVM) at 793 cm^{-1} above the optical branch are because of chemical substitution of heavier elements. The band observed at 837 cm^{-1} (y = 0.02) is seen in materials with aliovalent substitution and hence is due to internal deformation caused by charge differences.[26,27] The E(TO1) mode, A1(TO1), and broad peak A1(TO2) are due to BO_6 bending vibrations. The asymmetry peak at 519 cm^{-1} (for y = 0.02) corresponds to A1(TO) and E(TO) and at 718 cm^{-1} for A1(LO) and E(LO), and that at a high wavenumber is due to the presence of vibrations of oxygen octahedra.[32]

3.3. Microstructural Analysis. The SEM images of the $Ba_{1-x}Pr_{2x/3}Ti_{1-y}(Mo_{1/2}Nb_{1/2})_yO_3$ samples for various compositions are presented in Figure 7a−e. The figure displays a dense microstructure with minimal porosity and slight surface fusion of grains, except for the BTMN02 composition. The grain size has been calculated using ImageJ software. The average grain size for the lowest doping concentration (BTMN02) is 0.36 μm, which increases to 0.44 μm for BTMN04 and then to 0.49 μm for BTMN06. As the doping concentration increases further, the grain size decreases to 0.26 μm for BTMN08 and 0.25 μm for BTMN10. The average grain size for the lowest doping concentration (BTMN02) is 0.36 μm, which increases to 0.44 μm for BTMN04 and then to 0.49 μm for BTMN06. It is observed that initially the Mo and Nb-doped $BaTiO_3$ sample shows grain growth with increasing the doping percentage of Mo and Nb. A similar observation is also reported by Zhang et al. for the Co-doped $BaTiO_3$ system.[33] The increase in grain size can be attributed to ion diffusion by the dissolution and reprecipitation process during liquid phase sintering.[33−35] As the doping concentration increases further, the grain size decreases to 0.26 μm for BTMN08 and 0.25 μm for BTMN10. This crossover trend can be attributed to exceeding the solubility limit of the crystal lattice, which leads to secondary phase formation. These secondary phases pin the grain boundaries, restricting further growth and ultimately reducing the grain size.[36,37] While the liquid phase formed at higher doping levels can enhance initial densification, the simultaneous dopant segregation at grain boundaries and potential formation of secondary phases can effectively hinder grain boundary mobility, ultimately resulting in refined grain size.[36,37] These mechanisms have been also reported in other complex materials and justify our results.[33,36−38] Figure 7f shows the elemental mapping of the BTMN10 sample, where all of the constituent elements are

https://doi.org/10.1021/acsomega.5c04164
ACS Omega 2025, 10, 43779−43796

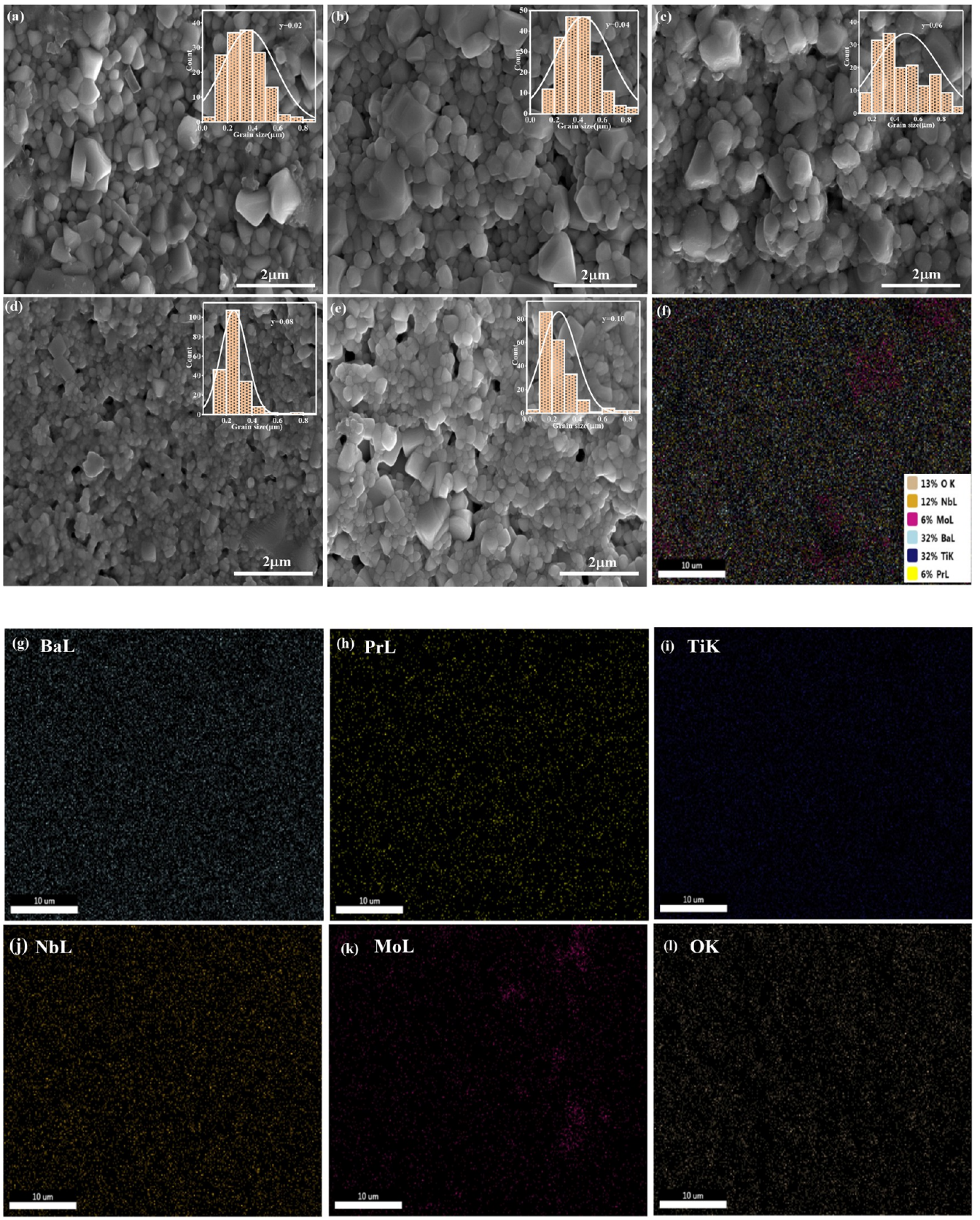

Figure 7. (a–e) Surface morphology SEM images along with grain size distribution histogram in the corresponding inset for $Ba_{1-x}Pr_{2x/3}Ti_{1-y}(Mo_{1/2}Nb_{1/2})_yO_3$ ceramics, (f) elemental mapping of the BTMN10 sample, and (g–l) mapping of the different elements for same composition.

https://doi.org/10.1021/acsomega.5c04164
ACS Omega 2025, 10, 43779–43796

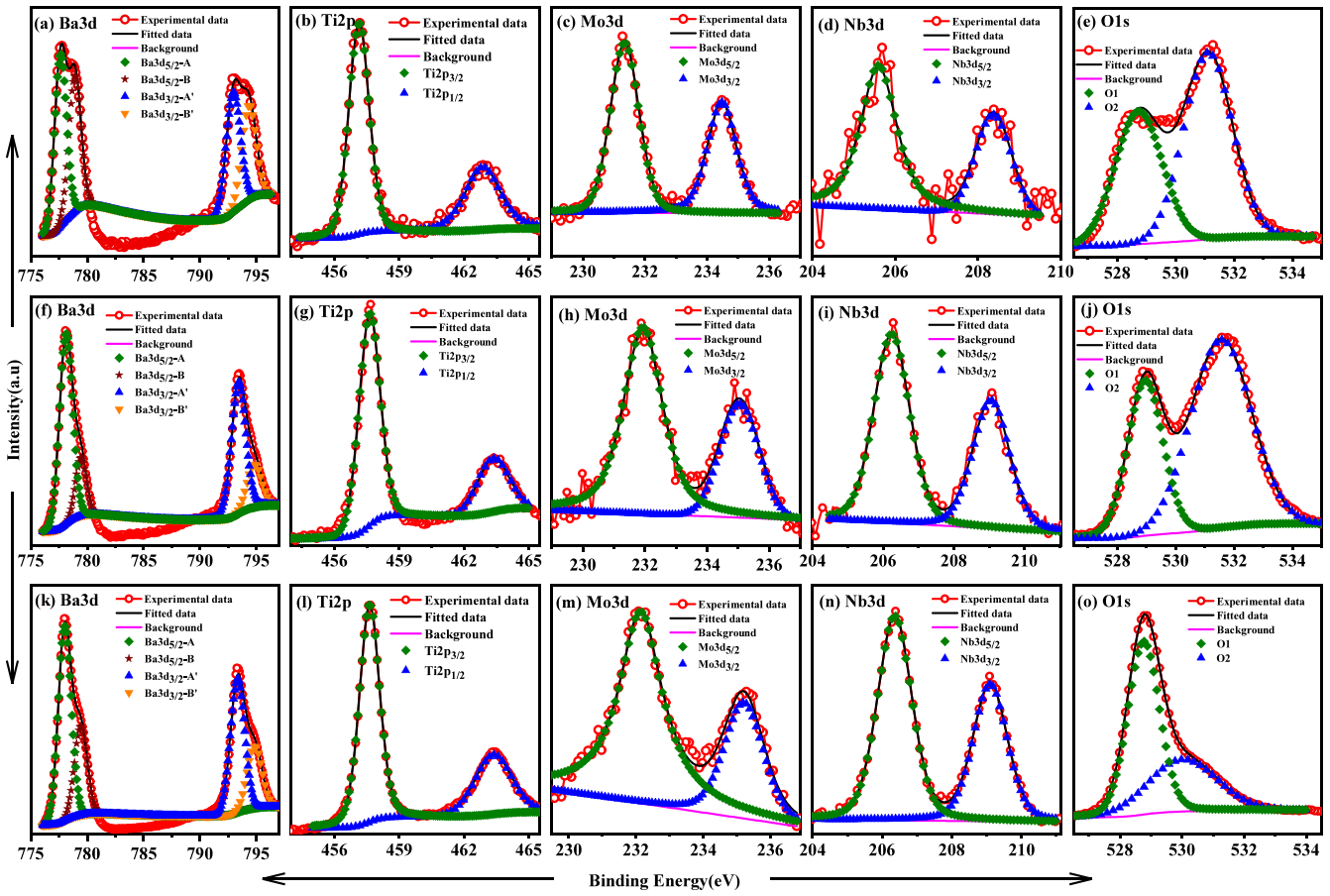

Figure 8. XPS spectra for different elements in $Ba_{1-x}Pr_{2x/3}Ti_{1-y}(Mo_{1/2}Nb_{1/2})_yO_3$ with x = 0.03, y = 0.04, 0.06, and 0.10. (a–e) BTMN04, (f–j) BTMN06, and (k–o) BTMN10 sample.

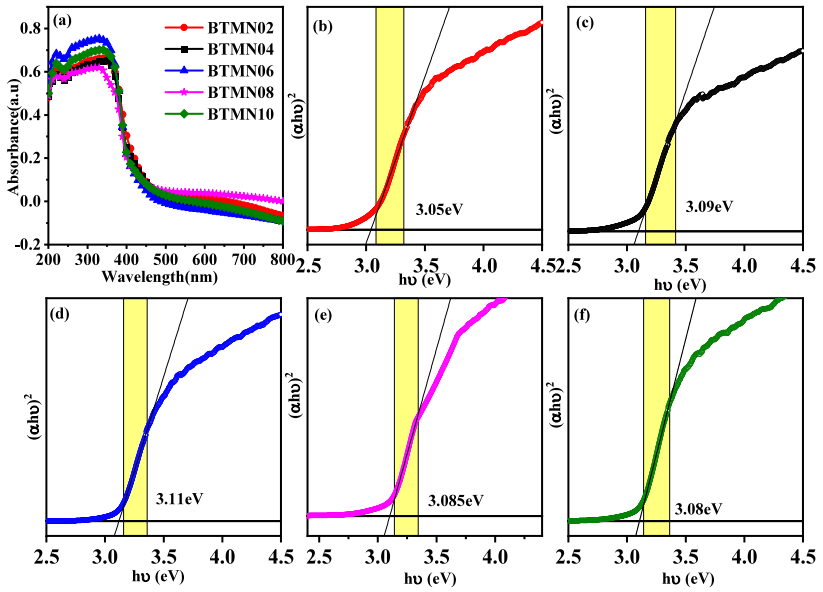

Figure 9. (a) Absorption spectra of $Ba_{1-x}Pr_{2x/3}Ti_{1-y}(Mo_{1/2}Nb_{1/2})_yO_3$ samples. (b) Tauc's plot of BTMN02, (c) BTMN04, (d) BTMN06, (e) BTMN08, and (f) BTMN10.

evenly distributed except for Mo, which concentrates in specific regions. This concentration may correspond to secondary phase $BaMoO_4$ and undissolved molybdenum oxide. Figure 7g–l illustrates the elemental distribution of Ba, Pr, Ti, Nb, Mo, and O in the BTMN10 composition, demonstrating an even distribution of each element.

3.4. X-ray Photoelectron Spectroscopy (XPS) Studies.

Figure 8 illustrates the XPS spectra of the $Ba_{1-x}Pr_{2x/3}Ti_{1-y}(Mo_{1/2}Nb_{1/2})_yO_3$ ceramics. Figure 8a–e

https://doi.org/10.1021/acsomega.5c04164
ACS Omega 2025, 10, 43779–43796

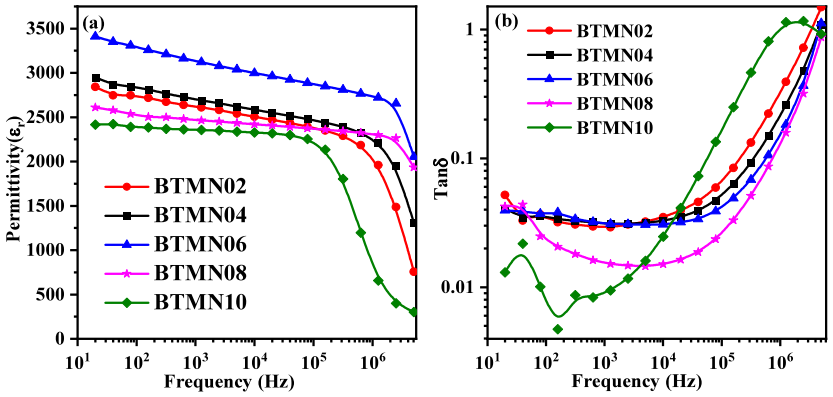

Figure 10. (a) Permittivity and (b) dielectric loss of $Ba_{1-x}Pr_{2x/3}Ti_{1-y}(Mo_{1/2}Nb_{1/2})_yO_3$ samples (x = 0.03, y = 0.02, 0.04, 0.06, 0.08, and 0.10) as a function of frequency from 20 Hz to 5 MHz, measured at room temperature.

shows the XPS plot of BTMN04, (f–j) of BTMN06, and (k–o) of BTMN10. The Ba 3d spectra have Ba $3d_{5/2}$ and Ba $3d_{3/2}$ peaks with each having two components marked as A, B and A′, B′, respectively. The peaks at 777.7 and 778.7 eV correspond to A and B of Ba $3d_{5/2}$ and the peaks at 793.1 and 794.2 eV to A′ and B′ of Ba-$3d_{3/2}$, respectively, for the BTMN04 sample. For BTMN06, A is at binding energy of 778.1 eV, B at 779.6 eV, A′ at 793.5 eV, and B′ at 795 eV. For BTMN10, peak A is at binding energy of 778 eV, B at 779.5 eV, A′ at 793.3 eV, and B′ 794.9.eV. The peaks A and A′ are assigned to the Ba^{2+} state of the perovskite lattice, whereas B and B′ peaks are due to surface contamination and Ba vacancy defects.[39,40] The Ti 2p spectra of Ti has Ti $2p_{3/2}$ peaks at 457.1, 457.6, and 457.7 eV and Ti $2p_{1/2}$ peaks at 462.9, 463.3, and 463.4 eV, respectively, corresponding to the compositions BTMN04, BTMN06, and BTMN10. The peak positions above indicate the presence of Ti 2p in the Ti^{4+} state. The Ti 2p peaks show minor shifts in binding energy with increasing doping concentrations but maintain a consistent peak shape without any broadening or the emergence of an additional peak; this behavior is characteristic of Ti in $BaTiO_3$.[41,42] The minor shift toward the higher binding energy with increasing doping concentration suggests a lower concentration of Ti ions, which is due to incorporation of dopant ions into the lattice.[20,43] The Mo 3d spectra have Mo -$3d_{5/2}$ and Mo $3d_{3/2}$ peaks with binding energies at 231.3 and 234.4 eV for BTMN04, at 231.9 and 235 eV for BTMN06, and at 232.1 and 235.2 eV for BTMN10.[44,45] These characteristic peaks are in accordance with the Mo^{6+} state and is attributed to the Mo–O bond.[41,46] The Nb -3d spectra have two peaks of Nb -$3d_{5/2}$ and Nb $3d_{3/2}$ states having binding energies of 205.6 and 208.37 eV for BTMN04, 206.27 and 209.08 eV for BTMN06, and 206.37 and 209.08 eV for BTMN10. These peaks are assigned to Nb^{5+} of the Nb 3d state.[42,47] The Ti 2p, Mo 3d, and Nb 3d peaks shift on changing doping concentration because of charge distribution.[41,46] Pr 3d peaks are not detectable in the XPS spectra because of the very low concentration. The XPS spectra of O 1s peaks are marked as O1 and O2 at binding energies 528.6 and 531.2 eV for BTMN04, 529 and 531.8 eV for BTMN06, and 528.7 and 530.7 eV for BTMN10. The O1 peak is attributed to the lattice oxygen, whereas O2 is related to oxygen vacancies or surface absorbed oxygen.[48–50] The reduction of the higher binding energy peak around 531 eV suggests a decrease in the amount of oxygen vacancies.[20] The slight shift of the oxygen vacancy peak to a lower binding energy further indicates a reduction in the level of oxygen vacancies.[49]

3.5. Band Gap Analysis. Figure 9a displays the absorption spectra of $Ba_{1-x}Pr_{2x/3}Ti_{1-y}(Mo_{1/2}Nb_{1/2})_yO_3$ samples recorded in the wavelength range of 200–800 nm, which is used to calculate the optical band gap of all the samples. The spectra show a broad absorption band below 350 nm indicating absorption in the low-wavelength region of the spectrum. Compositions BTMN06 and BTMN10 show higher absorption in the UV region that may be attributed to coupling of the doped ions with oxygen vacancies and presence of intermediate defect states.[51] The indirect band gap of a material is calculated from Tauc's equation $(\alpha h\nu) = A(h\nu - E_g)^{1/2}$, where α is the absorption coefficient, $h\nu$ is the incident photon energy, A is a proportionality constant, and E_g is the band gap. The intercept of the tangent line drawn from the linear portion of $(\alpha h\nu)^2$ versus $h\nu$ plot gives the value of the band gap.[52] Figure 9b–f shows the optical band gap plots. For BTMN02, the obtained band gap is 3.05 eV, which is significantly lower than the band gap of undoped $BaTiO_3$ (E_g = 3.31 eV) ceramic. All compositions in this work show a lower band gap than the band gap of undoped $BaTiO_3$. The reduced band gap in (Pr, Nb, Mo)-doped $BaTiO_3$ can be attributed to new donor levels near the conduction band and presence of defect states.[53] The partially filled 4f orbitals of Pr interact with the conduction and valence bands, resulting in localized states that allow for electronic transitions at lower energies. Similarly, Mo and Nb create intermediate states near the conduction band minimum, which requires less energy and results in lower band gap.[50] The band gaps increase to 3.09 eV for BTMN04 and then to 3.11 eV for BTMN06. On further increasing the concentration, the band gaps decrease to 3.085 and 3.08 eV for BTMN08 and BTMN10, respectively. A slight change in band gap on changing doping concentration may be attributed to reduced oxygen vacancies.[54] The reduction of oxygen vacancies by (Mo, Nb) doping is confirmed by XPS spectra, as shown in Figure 8. The reduced oxygen vacancies with increasing the dopant concentration may be due to additional positive charges. The dopants with higher oxidation states (Mo^{6+}) add two extra charges compared to Ti^{4+} ion. Thus, a number of oxygen vacancies are reduced that also cause a decrease in the intermediate states.[55] The change in band gap with concentration can also be due to modified lattice distortion in the structure, which changes the bond lengths and bond angles because of different ionic sizes.[56]

https://doi.org/10.1021/acsomega.5c04164
ACS Omega 2025, 10, 43779–43796

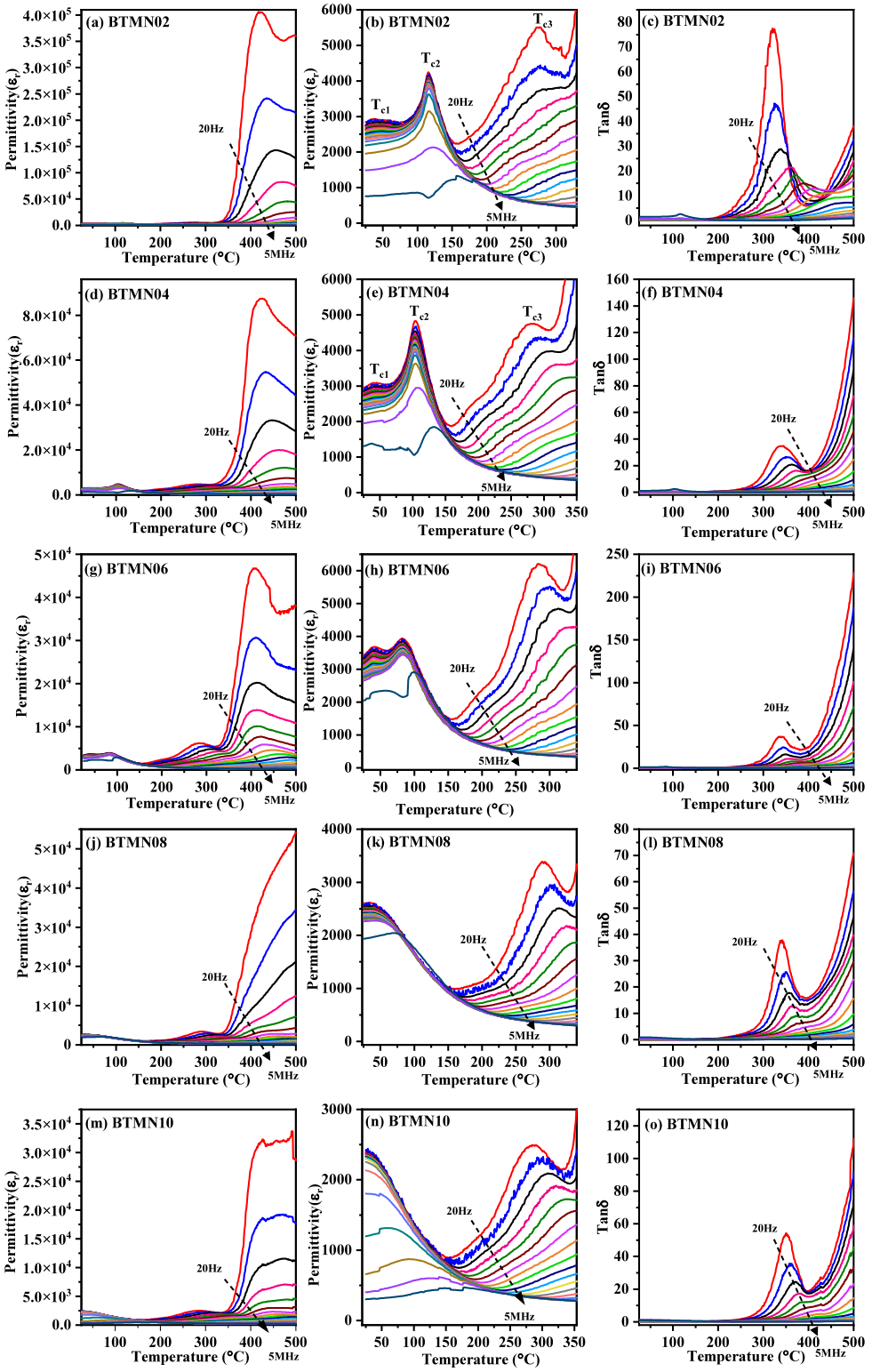

Figure 11. Temperature-dependent permittivity of $Ba_{1-x}Pr_{2x/3}Ti_{1-y}(Mo_{1/2}Nb_{1/2})_yO_3$ ceramic as a function of frequency from 20 Hz to 5 MHz and temperature up to 500 °C for (a) BTMN02, (d) BTMN04, (g) BTMN06, (j) BTMN08, and (m) BTMN10 composition. Temperature-dependent permittivity plot of the samples for temperature up to 300 °C showing transition temperature for (b) BTMN02, (e) BTMN04, (h) BTMN06, (k) BTMN08, and (n) BTMN10. Temperature-dependent dielectric loss (c, f, i, l, o) for all compositions (c) BTMN02, (f) BTMN04, (i) BTMN06, (l) BTMN08, and (o) BTMN10.

3.6. Dielectric Analysis. The behavior of dielectric permittivity (ε_r) with temperature and frequency is a critical factor of dielectrics for their application in capacitors, sensors, and tunable devices. Figure 10a shows the plots of the frequency-dependent relative permittivity (ε_r) for different compositions of $Ba_{1-x}Pr_{2x/3}Ti_{1-y}(Mo_{1/2}Nb_{1/2})_yO_3$ samples (x = 0.03, y = 0.02, 0.04, 0.06, 0.08, and 0.10) measured at room temperature, in the frequency range 20 Hz to 1 MHz. At low

https://doi.org/10.1021/acsomega.5c04164
ACS Omega 2025, 10, 43779−43796

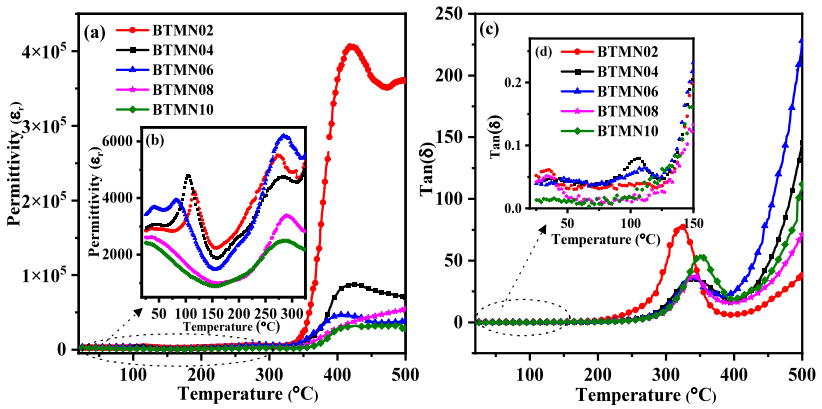

Figure 12. (a) Temperature-dependent permittivity and (c) dielectric loss of $Ba_{1-x}Pr_{2x/3}Ti_{1-y}(Mo_{1/2}Nb_{1/2})_yO_3$ at 20 Hz for compositions y = 0.02 to y = 0.10. Insets (b) and (d) show the enlarged view of the "ε_r−T" curve at a lower range of temperature.

frequencies (20 Hz to 1 kHz), samples exhibit very high dielectric permittivity due to their ferroelectric or relaxor nature and domain wall motion. Because of the combined effects of many polarizations including interfacial, ionic, dipolar, electronic, and space charge, the sample exhibits increased permittivity at lower frequencies.[57] The permittivity values gradually drop as the frequency is increased from 20 Hz to 100 kHz for all of the samples. At the low frequency zone, a plateau-like region is discovered, and it was found that the plateau-region widened as the doping concentration is increased. The dielectric permittivity (ε_r) of the material decreases with increasing frequency to 1000 kHz due to the inability of slower polarization mechanisms to respond effectively to the rapidly oscillating electric field.[57−59] This frequency-dependent behavior is characteristic of dielectric materials and reflects the inherent polarization dynamics and dispersive nature of the ceramic system under investigation. Additionally, the ceramics exhibit a characteristic relaxor behavior, evidenced by the frequency-dependent shift of the temperature at which maximum permittivity (T_m) occurs and the dielectric peaks broaden. These features point to a diffuse phase transition, commonly associated with disordered ferroelectric systems.[60,61] It is observed that, as the $(Mo_{1/2}Nb_{1/2})$ content in $Ba_{1-x}Pr_{2x/3}Ti_{1-y}(Mo_{1/2}Nb_{1/2})_yO_3$ is increased, the permittivity is also enhanced and reaches its maximum value for composition y = 0.06, and later, it starts decreasing for higher doping content. For BTMN02, the ε_r value is 2840.46 at 20 Hz, which is increased to 3408.7 for composition BTMN06. However, it shows a decreased value (ε_r = 2609) for composition BTMN08. For composition BTMN10, the ε_r value is further reduced to 2417.3 at 20 Hz. This trend in dielectric permittivity with increased $(Mo_{1/2}Nb_{1/2})$ content in $Ba_{1-x}Pr_{2x/3}Ti_{1-y}(Mo_{1/2}Nb_{1/2})_yO_3$ can be related to changes in crystal structure and phase change.[62] Figure 10b shows the variation of dielectric loss with frequency for all of the compositions. It is observed that dielectric loss at room temperature for composition BTMN02 is 0.052 and reduced to 0.039 for composition BTMN06. The dielectric loss for all the samples is found to be less than 0.055 in the frequency range 20 Hz to 100 kHz. Beyond 100 kHz, an abrupt increase in dielectric loss is observed.

Figure 11 shows the temperature-dependent dielectric permittivity and loss, from RT to 500 °C, for all the compositions of $Ba_{1-x}Pr_{2x/3}Ti_{1-y}(Mo_{1/2}Nb_{1/2})_yO_3$ with varying the test frequencies from 20 Hz to 0.5 MHz. It is observed that composition BTMN02 has three dielectric anomalies located at 37, 115, and 274 °C. According to Figure 11b, the permittivity value for frequency 20 Hz first increases (from ε_r = 2840.5 to 2933.6) with increasing temperature and at temperature (T_{c1}) 37 °C, it shows a small peak. Above 37 °C, it slightly decreases but again starts increasing and shows another peak at 115 °C (T_{c2}) temperature with increased permittivity (ε_r = 4243.2). The dielectric peak "T_{c2}" is due to thermal evolutions of polar nanoregions and shows a weak frequency dispersion.[62] The third dielectric peak (T_{c3}) is at 274 °C for a frequency of 20 Hz, which shows much variation with frequency. The "T_{c3}" peak is attributed to defect dipole relaxations. "T_{c3}" shifts toward higher temperatures from 274 to 305 °C for higher frequency (10 kHz) due to polarization dynamics and is a hallmark of materials exhibiting relaxor ferroelectric behavior or diffuse phase transitions.[20] As shown in Figure 11b,e,h,k,n, most compositions exhibit three distinct dielectric anomalies, with the exception of BTMN08 and BTMN10, where the first transition temperature (T_{c1}) appears to shift below room temperature and thus falls outside the measurement range of this study. The first two anomalies are likely linked to intrinsic phase transitions associated with the material's crystal structure. The dielectric peaks are directly related to the phase transition behavior, which is driven by changes in the crystal structure and polarization mechanisms with temperature.[20] It is also observed that dielectric peak "T_{c2}" is suppressed with increased $(Mo_{1/2}Nb_{1/2})$ doping, and the "ε_r−T" curve becomes more flattened. This shows improved dielectric temperature stability of $BaTiO_3$ with $(Mo_{1/2}Nb_{1/2})$ doping.[63] Aliovalent dopants generate local random fields that impair the long-range ferroelectric order and regularity of the polarization response. This broadens the phase transition to make it diffuse along with a frequency-dependent shift. At higher frequencies, the bigger size polar nanoregions contribute less, lowering the dielectric value.

Figure 12 depicts the temperature-dependent permittivity and dielectric loss of $Ba_{1-x}Pr_{2x/3}Ti_{1-y}(Mo_{1/2}Nb_{1/2})_yO_3$ for compositions y = 0.02 to y = 0.10 at a selected frequency of 20 Hz It is observed that permittivity increases with increasing the $(Mo_{1/2}Nb_{1/2})$ doping concentration, and composition y = 0.06 shows the highest room-temperature dielectric permittivity (ε_r = 3408.7 measured at 20 Hz). Further doping causes a slight decrease in permittivity. The dielectric loss decreases with increasing the $(Mo_{1/2}Nb_{1/2})$ doping and shows the lowest value (tan δ = 0.039) for composition y = 0.06. Figure 12c

https://doi.org/10.1021/acsomega.5c04164
ACS Omega 2025, 10, 43779−43796

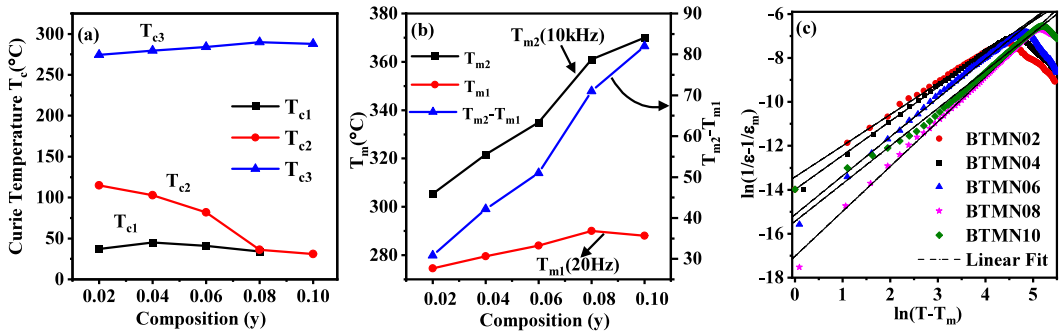

Figure 13. (a) Curie temperature for $Ba_{1-x}Pr_{2x/3}Ti_{1-y}(Mo_{1/2}Nb_{1/2})_yO_3$ as a function of composition measured at 20 Hz frequency. (b) Dielectric peak temperatures (T_{m1} and T_{m2}) as a function of composition at the frequencies 20 Hz and 10 kHz. (c) Modified Curie–Weiss law plot for finding diffuseness parameter "γ" at 1 kHz frequency from RT to 350 °C.

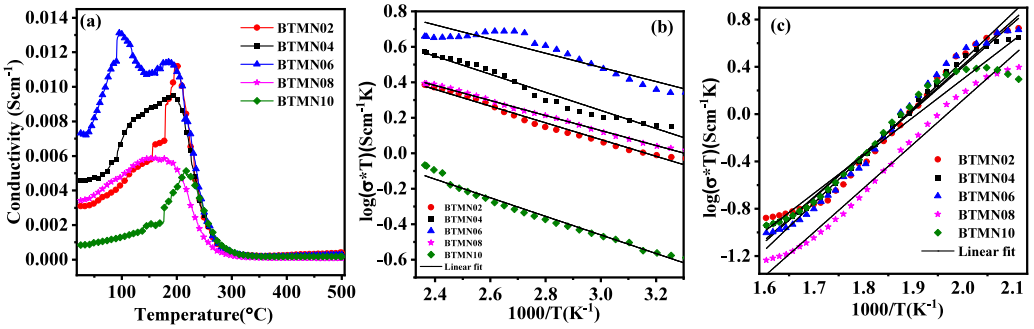

Figure 14. (a) Conductivity versus temperature plot of $Ba_{1-x}Pr_{2x/3}Ti_{1-y}(Mo_{1/2}Nb_{1/2})_yO_3$ compositions at 3.16×10^5 frequency. (b) Arrhenius plot for all the compositions in the temperature range 25 to 150 °C at 3.16×10^5 frequency. (c) Arrhenius plot for all the composition in the temperature range 200 to 350 °C at 3.16×10^5 frequency.

illustrates the dielectric loss, which is nearly constant between RT and 200 °C. All compositions show low dielectric loss (less than 0.2) from room temperature to 150 °C. Above 200 °C, the dielectric loss starts increasing. Furthermore, as frequency increases, the tanδ peak location moves toward higher temperatures. It is possible that increasing defects, leakage current production from thermally accelerated charge carrier movement, and defect polarization are the causes of the rapid growth in dielectric loss above 200 °C.[61]

Figure 13 depicts the "T_c", "T_m", and modified Curie–Weiss law plot. $Ba_{1-x}Pr_{2x/3}Ti_{1-y}(Mo_{1/2}Nb_{1/2})_yO_3$ ceramics with composition BTMN02 shows "T_{c2}" at 115 °C, which decreases with increasing the $(Mo_{1/2}Nb_{1/2})$ content, and composition BTMN10 shows "T_{c2}" at 31 °C. The $Ba_{1-x}Pr_{2x/3}Ti_{1-y}(Mo_{1/2}Nb_{1/2})_yO_3$ ceramics demonstrate notably high dielectric permittivity at temperatures above 350 °C and frequencies below 1 kHz. This trend is characteristic of Maxwell–Wagner interfacial polarization, which originates from charge accumulation at interfaces such as grain boundaries or regions with differing electrical conductivity.[58] In contrast, the lower permittivity observed between room temperature and 350 °C may reflect limited space charge mobility or less pronounced interfacial polarization under those conditions. While dipolar polarization typically decreases with rising temperature due to thermal agitation, the enhanced mobility of charge carriers at elevated temperatures can amplify interfacial polarization effects, thereby contributing to the observed increase in permittivity.[60] The difference in peak temperatures (T_{m1} and T_{m2}) at two frequencies can be used to determine the relative relaxor behavior of different compositions. The dielectric peak temperature is represented by the symbols "T_{m1}" for 20 Hz and "T_{m2}" for 10 kHz. The difference ($T_{m2} - T_{m1}$) is calculated and plotted as a function of composition, as shown in Figure 13b. It also shows the variations of peak temperatures (T_{m1} and T_{m2}) as a function of composition. It is found that the difference ($T_{m2} - T_{m1}$) increases with increasing $(Mo_{1/2}Nb_{1/2})$ doping content. The increasing difference in peak temperature ($T_{m2} - T_{m1}$) shows an enhanced relaxor character.[63] In order to further identify the relaxation behavior of ceramics, the diffuseness parameter (γ) has been calculated as per eq 5, using the modified Curie–Weiss law by plotting the graph between $\ln(T - T_m)$ versus $\ln(1/\varepsilon_r - 1/\varepsilon_m)$ and by fitting the plot with the linear equation above and slope gives the value of γ. The obtained results are listed in Figure 13c. The diffuseness parameter (γ) for composition $y = 0.02$ is 1.4, which increases with increasing doping content, caused by enhanced cation disorder by B-site replacements with $(Mo_{1/2}Nb_{1/2})$.[64,65] The obtained values of diffuseness parameter γ is higher than 1 for all the doped compositions, which confirms that dielectric behavior is between normal and relaxor ferroelectric. These results clearly deviate from the expected Curie–Weiss behavior and prove that the produced ceramic by $(Mo_{1/2}Nb_{1/2})$ doping is relaxor ferroelectric. The γ value rises from 1.4 to 2 for $y = 0.08$ and then falls to 1.7 for $y = 0.1$. It is noticed that composition $y = 0.08$ has the strongest relaxor ferroelectric qualities, and the fact that it is 2 suggests that ceramic is ideally relaxor ferroelectric.[20,60] The value of γ increases with increasing Mo and Nb doping levels, suggesting a shift from abrupt, first-order phase transitions to more diffuse, second-order-like transitions.[66] A more diffuse phase transition results from $(Mo_{1/2}Nb_{1/2})$ doping due to distortion of the lattice and

https://doi.org/10.1021/acsomega.5c04164
ACS Omega 2025, 10, 43779–43796

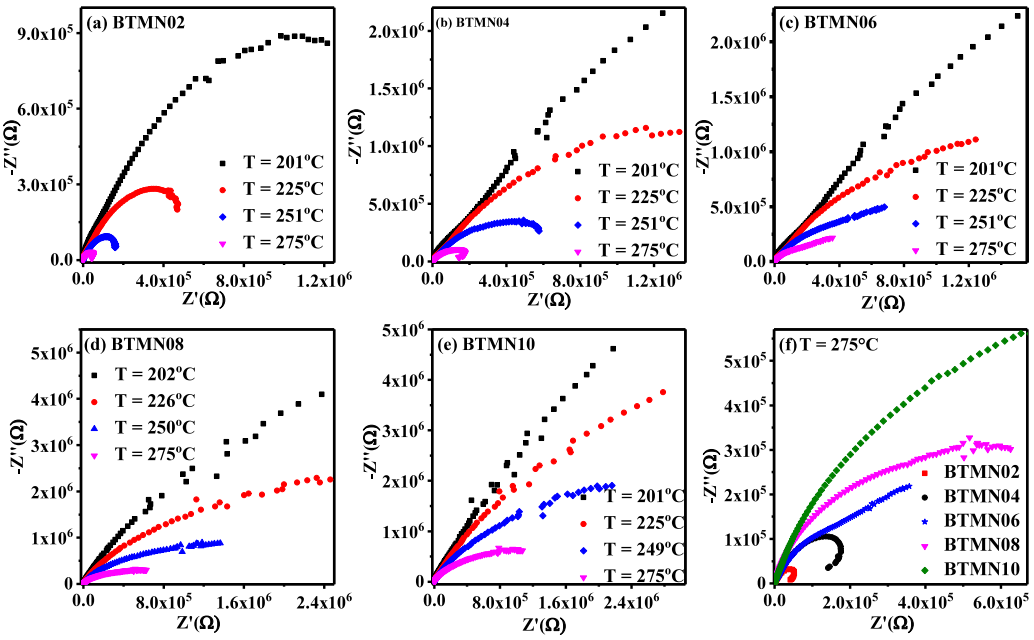

Figure 15. (a–e) Nyquist plots for $Ba_{1-x}Pr_{2x/3}Ti_{1-y}(Mo_{1/2}Nb_{1/2})_yO_3$ compositions (y = 0.02 to 0.10), measured at different temperatures. (f) Composition variation of Nyquist plots measured at 275 °C temperature.

disruption of the long-range ferroelectric order. Because of the different electronegativities and valences of cations, doping introduces dipole–dipole interactions that are competitive. The long-range ferroelectric order is weakened by this frustration, which widens the phase transition.

3.7. Electrical Impedance and Conductivity Analysis.

Figure 14a shows the conductivity of $Ba_{1-x}Pr_{2x/3}Ti_{1-y}(Mo_{1/2}Nb_{1/2})_yO_3$ compositions with varying temperatures. Conductivities of samples were calculated using the resistivity value measured from room temperature to 500 °C. Here, we observed that the resistivity decreases with increasing the temperature and attained a minimum value, which is different for different compositions. The thermally activated electrons from donor levels or oxygen vacancies contribute significantly to conduction, and thus conductivity increases with increasing the temperature.[66,67] When resistivity is converted in conductivity values, we observed a peak around the temperature 200 °C, as shown in Figure 14a. This shows that all compositions show a semiconducting nature. It is found that with increasing the doping content, the conductivity increases and the maximum value is obtained below 100 °C temperature for composition y = 0.06. This suggests that doping increases the semiconducting nature of $BaTiO_3$ ceramics.[66] It can be attributed to the introduction of donor states, enhanced free carrier concentration, and structural modifications that influence charge transport mechanisms. This $(Mo_{1/2}Nb_{1/2})$ doping adds extra electrons to the conduction band in order to maintain the charge neutrality. These extra electrons considerably increase the free carrier concentration, which increases the electrical conductivity. The activation energy of ceramics determines the energy barrier in the conduction processes. Doping with Nb and Mo greatly influences the activation energy. For activation energy calculation, two plots are drawn in two different temperature ranges (25–150 and 200–350 °C). For calculation of activation energy "E_a", the Arrhenius equation is plotted in $1000/T$ (in K^{-1}) versus $\mathrm{Log}(\sigma^*T)$ (S cm^{-1} K). The plot obtained between $1000/T$ (in K^{-1}) and $\mathrm{Log}(\sigma^*T)$ (S cm^{-1} K) is fitted using a linear fit in origin. The value of the slope obtained from the fitting has been used for calculating the activation energy with the following formula: $\frac{-E_a}{K_B}$ = slope, where E_a is the activation energy and K_B is the Boltzmann's constant. The activation energy shows different behaviors according to structural phases of doped $BaTiO_3$ ceramics.[59,66] For composition y = 0.02 and y = 0.04, the activation energy increases from 0.0405 to 0.0439 eV in the low-temperature region (25 to 150 °C). Dopants such as Mo^{6+} and Nb^{5+}, when introduced at the Ti^{4+} site in $BaTiO_3$, induce lattice distortions and alter the ceramic's localized fields. At lower doping concentrations (y = 0.06), the structure remains predominantly cubic and the material exhibits a relatively low activation energy of 0.0344 eV. This may be associated with enhanced ionic transport or the presence of shallow defect states that facilitate charge migration. As the dopant concentration increases (y = 0.10), the activation energy rises slightly to 0.0451 eV in the temperature range (25 to 150 °C), potentially due to the formation of deeper trap states, increased structural disorder, or reduced carrier mobility. The activation energy increases from 0.0344 eV for composition y = 0.06 to 0.0451 eV for composition y = 0.10. Importantly, the influence of oxygen vacancies and localized electric fields on charge transport is complex, and changes in activation energy cannot be attributed solely to their presence or concentration. Instead, a nuanced interplay of structural and defect-related factors governs the observed conduction behavior. The Nb^{5+} and Mo^{6+} dopants influence the electrical conduction behavior of $BaTiO_3$ ceramics through distinct yet interrelated mechanisms. Nb^{5+} generally acts as a donor dopant, introducing additional free electrons that facilitate electronic conduction and tend to lower the activation energy. In contrast, Mo^{6+} can promote the formation of oxygen vacancies, which enhances ionic conduction pathways. Together, these dopants modify the defect sites and transport dynamics within the material. For the composition with y = 0.06, the activation energy is relatively higher (0.345 eV), possibly due to the presence of deeper trap

https://doi.org/10.1021/acsomega.5c04164
ACS Omega 2025, 10, 43779–43796

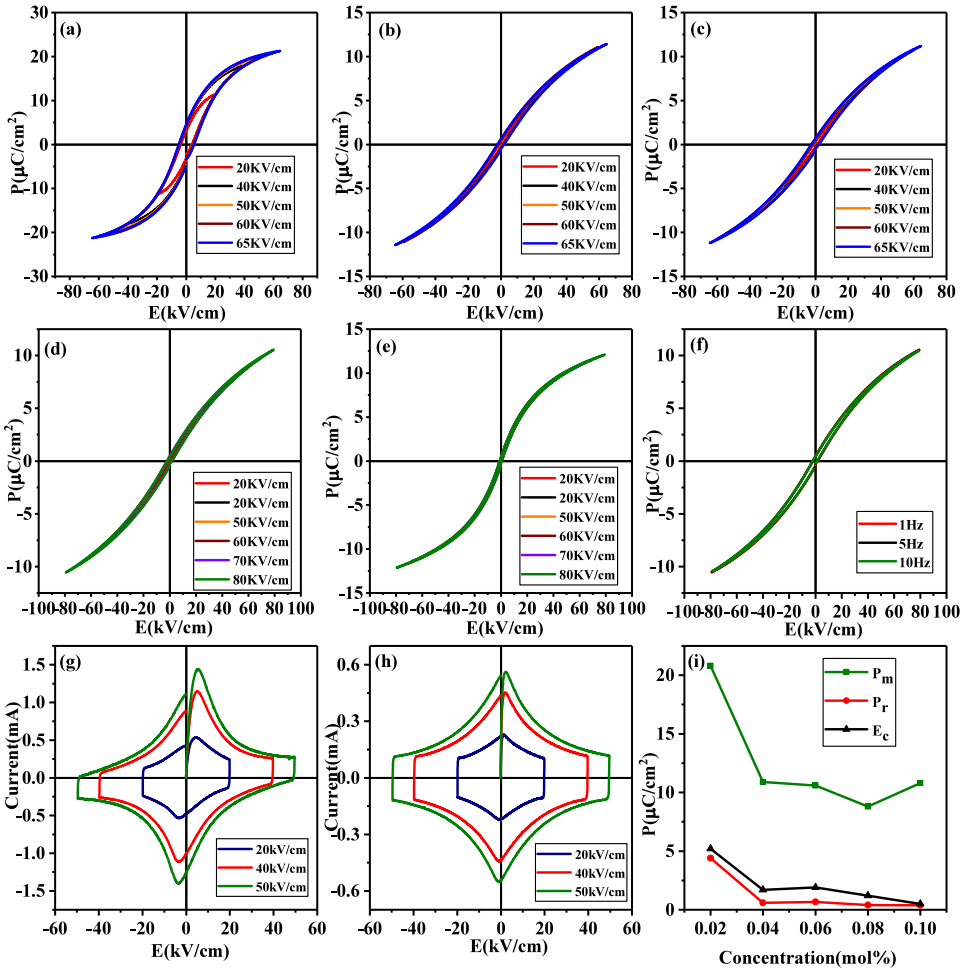

Figure 16. (a) P−E hysteresis loop of the samples with y = 0.02, (b) y = 0.04, (c) y = 0.06, (d) y = 0.80, (e) y = 0.10, (f) P−E loop of y = 0.08 sample at 80 kV/cm electric field, (g) I−E loop at 10 Hz of y = 0.02, (h) I−E loops at 10 Hz of y = 0.10, and (i) variation of P_m, P_r, and E_c values from the P−E loop of various compositions.

states or limited charge carrier mobility. As the dopant concentration increases (y = 0.10), the activation energy decreases to 0.277 eV, which may indicate a transition toward more efficient carrier hopping or a shift in the dominant conduction mechanism. In the temperature range of 200−350 °C, conduction is increasingly governed by thermally activated processes, where more charge carriers gain sufficient energy to overcome the potential barriers, resulting in enhanced conductivity.[20,57,60]

In order to further investigate the conduction mechanism of $Ba_{1-x}Pr_{2x/3}Ti_{1-y}(Mo_{1/2}Nb_{1/2})_yO_3$ samples, the impedance spectrum was tested from room temperature to 300 °C. Nyquist plots (Z' vs Z'') for $Ba_{1-x}Pr_{2x/3}Ti_{1-y}(Mo_{1/2}Nb_{1/2})_yO_3$ (y = 0.02 to 0.10) compositions are shown in Figure 15a−e. The Nyquist plot at selected temperatures is compared for all the compositions in Figure 15f. The arc in the Nyquist plot becomes smaller at higher temperatures, which shows an increase in conductivity of ceramics. At higher temperatures, more electrons are thermally excited from the valence band to the conduction band in the bulk. Grain boundaries often trap charges, creating a potential barrier that impedes conduction. At higher temperatures, the trapped charges gain sufficient energy to overcome this barrier, reducing grain boundary resistance. As observed in Figure 15f, the arc diameters in the Nyquist plots increase with higher concentrations of ($Mo_{1/2}$, $Nb_{1/2}$) codoping, indicating an enhancement in the material's total resistive components— particularly within the grain and grain boundary regions. Contrary to the conventional association of increased resistance with oxygen vacancy proliferation, the Mo and Nb codoping in $BaTiO_3$-based ceramics reduces oxygen vacancy concentration due to effective charge compensation provided by high-valence donor dopants (Mo^{6+} and Nb^{5+}). The suppression of oxygen vacancies limits defect-mediated conduction paths, resulting in a lower carrier concentration. Additionally, the introduction of dopants may cause lattice distortion and potential barrier formation at the grain boundaries, which further impedes charge carrier transport. Collectively, these effects contribute to an increased bulk and interfacial resistance, reflected in the enlarged impedance arcs.[65,67,68]

3.8. Ferroelectric Analysis. Figure 16a−f illustrates the polarization−electric field (P−E) hysteresis loops of the $Ba_{1-x}Pr_{2x/3}Ti_{1-y}(Mo_{1/2}Nb_{1/2})_yO_3$ (x = 0.03) ceramics at room temperature. With increasing dopant concentration, the hysteresis loop becomes slimmer, indicating the materials' progression toward relaxor ferroelectric state. The measured maximum polarization (P_m) values at an electric field of 60 kV/cm and frequency of 1 Hz are 20.8, 10.9, 10.6, 8.8, and 10.8 $\mu C/cm^2$ for compositions with y = 0.02, 0.04, 0.06, 0.08, and 0.10, respectively. The corresponding remanent polarization

https://doi.org/10.1021/acsomega.5c04164
ACS Omega 2025, 10, 43779−43796

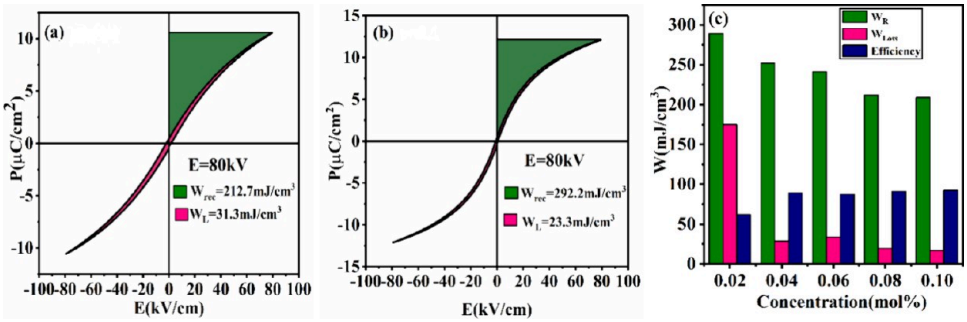

Figure 17. Energy storage performance of (a) BTMN08 at 80 kV/cm and 1 Hz and (b) BTMN10. (c) Variation in W_R, W_{Loss}, and efficiency values with composition.

(P_r) values are 4.47, 0.60, 0.67, 0.48, and 0.38 $\mu C/cm^2$ for these compositions, while the coercive field (E_c) values are found to be 5.2, 1.7, 1.9, 1.2, and 0.5 kV/cm, respectively, with increasing dopant concentrations. For samples with higher dopant levels, the P_m and P_r values at 80 kV/cm field at 1 Hz measuring frequency are 10.5 and 0.46 $\mu C/cm^2$ ($y = 0.08$) and 12.1 and 0.44 $\mu C/cm^2$ (for $y = 0.10$), respectively. This observed trend of decline in both P_m and P_r values with increased dopant concentration suggests the development of relaxor characteristics attributed to the disruption in long-range dipole ordering caused by dopant-induced local structural disorder.[69,70] Figure 16f presents the frequency dependence of the polarization for the BTMN08 sample at a fixed electric field of 80 kV/cm. The reduction in E_c with higher doping is advantageous for energy storage applications as E_c reflects the domain wall mobility under an applied field. A lower E_c implies reduced domain wall pinning, facilitating domain switching with minimal energy dissipation.[34,66] The decrease in E_c and P_r is associated with enhanced energy storage efficiency and is attributed to the grain size changes and defects that act as pinning centers. Similar results are also reported in literature.[8,66,71,72] This phase transition from normal ferroelectric to relaxor ferroelectric also plays a role in enhanced energy storage. Figure 16g,h illustrates the current electric field (I−E) characteristics of BTMN02 and BTMN10 samples at 10 Hz under varying electric fields. In the I−E loop, the coercive field is the electric field magnitude at which maximum domain switching occurs, resulting in a sharp current peak due to rapid domain reorientation. These peaks in the I−E loop are consistent with literature where domain switching induces a pronounced current peak validating the ferroelectric behavior.[73,74]

The highest values for W_R and η were observed in samples with increased dopant concentrations under a high electric field of 80 kV/cm for a measuring frequency of 1 Hz. The thickness of all the samples for measurement lies between 1100 and 1250 μm. Figure 17a,b presents the energy storage characteristics of BTMN08 and BTMN10, giving W_R values of 317.7 and 292.2 mJ/cm^3 with efficiencies of 91 and 92.6%, respectively, at 80 kV/cm field and 1 Hz frequency. Figure 17c further illustrates the trend in W_R, W_{Loss}, and η as a function of dopant concentration at 60 kV/cm field and 1 Hz frequency, showing that W_R and W_{Loss} decrease with increasing dopant levels, whereas η increases. The recoverable energy density and efficiency for the BTMN02 are 289 mJ/cm^3 and 62.2% at 60 kV/cm field and 1 Hz frequency, which change to 209.6 mJ/cm^3 and 92.4% for BTMN10. The efficiency is greater than 85% for all the compositions when the electric field is more than 60 kV/cm, indicating great suitability of developed compositions for dielectric energy storage applications.

4. CONCLUSIONS

$Ba_{1-x}Pr_{2x/3}Ti_{1-y}(Mo_{1/2}Nb_{1/2})_yO_3$ ceramics were successfully synthesized and systematically investigated for their structural, dielectric, and energy storage properties. The introduction of dopants Pr, Mo, and Nb effectively disrupted long-range ferroelectric order, facilitating the formation of polar nanodomains and inducing relaxor ferroelectric behavior. The BTMN06 composition shows high dielectric permittivity and low dielectric loss. The Curie temperature (T_c) shifts downward with increasing doping, indicating enhanced relaxor characteristics, further supported by increasing diffusion parameters and broadened dielectric peaks. Energy storage studies highlighted BTMN08 as the optimum composition with a peak recoverable energy density of 317.7 mJ/cm^3 and 91% efficiency at 80 kV/cm, while all compositions show efficiencies >85% under high electric fields. These findings underscore the potential of $Ba_{1-x}Pr_{2x/3}Ti_{1-y}(Mo_{1/2}Nb_{1/2})_yO_3$ ceramics for advanced energy storage applications due to their high energy density, efficiency, and tunable dielectric properties.

■ ASSOCIATED CONTENT

Data Availability Statement

The authors confirm that the data supporting the findings of this study are available within the article.

■ AUTHOR INFORMATION

Corresponding Author

Akhilesh Kumar Singh − *School of Materials Science and Technology, Indian Institute of Technology (Banaras Hindu University), Varanasi 221005, India;* orcid.org/0000-0001-8729-7318; Email: aksingh.mst@iitbhu.ac.in

Authors

Deep Mala − *School of Materials Science and Technology, Indian Institute of Technology (Banaras Hindu University), Varanasi 221005, India*

Chandra Bhal Singh − *School of Materials Science and Technology, Indian Institute of Technology (Banaras Hindu University), Varanasi 221005, India;* orcid.org/0000-0002-8557-0752

Complete contact information is available at: https://pubs.acs.org/10.1021/acsomega.5c04164

https://doi.org/10.1021/acsomega.5c04164
ACS Omega 2025, 10, 43779−43796

Author Contributions

Deep Mala contributed to methodology, visualization, data curation and analysis, investigation, and writing—review and editing. Chandra Bhal Singh contributed to conceptualization, methodology, visualization, data curation and analysis, investigation, and writing—review. Akhilesh Kumar Singh contributed to methodology, visualization, data curation, resources, review, and editing. All authors read and approved the final manuscript.

Notes

The authors declare no competing financial interest.

■ ACKNOWLEDGMENTS

The authors are thankful to the Central Instrumental Facility, Indian Institute of Technology (Banaras Hindu University) for providing experimental facility such as XPS, SEM, and EDS. Deep Mala acknowledges IIT (BHU) for providing the institute SRF fellowship. The authors acknowledge DST-FIST support for SmartLab XRD facility.

■ REFERENCES

(1) Yan, F.; Qian, J.; Wang, S.; Zhai, J. Progress and Outlook on Lead-Free Ceramics for Energy Storage Applications. *Nano Energy* **2024**, *123*, No. 109394.

(2) Sun, Z.; Wang, Z.; Tian, Y.; Wang, G.; Wang, W.; Yang, M.; Wang, X.; Zhang, F.; Pu, Y. Progress, Outlook, and Challenges in Lead-Free Energy-Storage Ferroelectrics. *Adv. Electron. Mater.* **2020**, *6* (1), 1−34.

(3) Zhang, H.; Wei, T.; Zhang, Q.; Ma, W.; Fan, P.; Salamon, D.; Zhang, S. T.; Nan, B.; Tan, H.; Ye, Z. G. A Review on the Development of Lead-Free Ferroelectric Energy-Storage Ceramics and Multilayer Capacitors. *J. Mater. Chem. C* **2020**, *8* (47), 16648−16667.

(4) Jayakrishnan, A. R.; Silva, J. P. B.; Kamakshi, K.; Dastan, D.; Annapureddy, V.; Pereira, M.; Sekhar, K. C. Are Lead-Free Relaxor Ferroelectric Materials the Most Promising Candidates for Energy Storage Capacitors? *Prog. Mater. Sci.* **2023**, *132*, No. 101046.

(5) Hao, X. A Review on the Dielectric Materials for High Energy-Storage Application. *J. Adv. Dielectr.* **2013**, *03* (01), 1330001.

(6) Pattipaka, S.; Lim, Y.; Son, Y. H.; Bae, Y. M.; Peddigari, M.; Hwang, G. T. Ceramic-Based Dielectric Materials for Energy Storage Capacitor Applications. *Materials* **2024**, *17* (10), 2277.

(7) Guo, B.; Jin, F.; Li, L.; Pan, Z. Z.; Xu, X. W.; Wang, H. Design Strategies of High-Performance Lead-Free Electroceramics for Energy Storage Applications. *Rare Met.* **2024**, *43* (3), 853−878.

(8) Veerapandiyan, V.; Benes, F.; Gindel, T.; Deluca, M. Strategies to Improve the Energy Storage Properties of Perovskite Lead-Free Relaxor Ferroelectrics: A Review. *Materials* **2020**, *13* (24), 5742.

(9) Aoujgal, A.; Gharbi, W. A.; Outzourhit, A.; Ahamdane, H.; Ammar, A.; Tachafine, A.; Carru, J. C. Relaxor Behavior in $(Ba_{1-3x/2}Bi_x)(ZryTi_{1-y})O_3$ Ceramics. *Ceram. Int.* **2011**, *37* (7), 2069−2074.

(10) Sahu, D. R. *Multifunctional Ferroelectric Materials*; BoD−Books on Demand: 2021. .

(11) Ahn, C. W.; Hong, C. H.; Choi, B. Y.; Kim, H. P.; Han, H. S.; Hwang, Y.; Jo, W.; Wang, K.; Li, J. F.; Lee, J. S.; Kim, I. W. A Brief Review on Relaxor Ferroelectrics and Selected Issues in Lead-Free Relaxors. *J. Korean Phys. Soc.* **2016**, *68* (12), 1481−1494.

(12) Li, F.; Zhang, S.; Damjanovic, D.; Chen, L. Q.; Shrout, T. R. Local Structural Heterogeneity and Electromechanical Responses of Ferroelectrics: Learning from Relaxor Ferroelectrics. *Adv. Funct. Mater.* **2018**, *28* (37), 1−21.

(13) Toulouse, J. The Three Characteristic Temperatures of Relaxor Dynamics and Their Meaning. *Ferroelectrics* **2008**, *369* (1 Part 3), 203−213.

(14) Huang, Y.; Zhao, C.; Wu, B.; Wu, J. Multifunctional BaTiO3-Based Relaxor Ferroelectrics toward Excellent Energy Storage Performance and Electrostrictive Strain Benefiting from Crossover Region. *ACS Appl. Mater. Interfaces* **2020**, *12* (21), 23885−23895.

(15) Thakur, P.; Sharma, N.; Pathak, D.; Sharma, P.; Kishore, K.; Dhar, S.; Lal, M. State-of-Art Review on Smart Perovskites Materials: Properties and Applications. *Emergent Mater.* **2024**, *7* (3), 667−694.

(16) Merselmiz, S.; Hanani, Z.; Mezzane, D.; Spreitzer, M.; Bradeško, A.; Fabijan, D.; Vengust, D.; Amjoud, M.; Hajji, L.; Abkhar, Z.; Razumnaya, A. G.; Rožič, B.; Luk'yanchuk, I. A.; Kutnjak, Z. High Energy Storage efficiency and Large Electrocaloric e Ff Ect in Lead-Free BaTi0.89Sn0.11O3 ceramic. *Ceram. Int.* **2020**, *46*, 23867−23876.

(17) Khardazi, S.; Mezzane, D.; Amjoud, M.; Novak, N.; Choukri, E.; Lyubchyk, S.; Kutnjak, Z.; Rožič, B.; Terenchuk, S.; Lukyanchuk, I. Improved Thermal Stability of Dielectric Properties and Energy Storage Properties of Lead-Free Relaxor $Ba_{(1-x)}La_xTi_{0.89}Sn_{0.11}O_3$ Ceramics. *Ceram. Int.* **2025**, *51*, 22386.

(18) Ma, C.; Du, H.; Liu, J.; Kang, L.; Du, X.; Xi, X.; Ran, H. High-Temperature Stability of Dielectric and Energy-Storage Properties of Weakly-Coupled Relaxor (1−x)BaTiO3-XBi(Y1/3Ti1/2)O3 Ceramics. *Ceram. Int.* **2021**, *47* (17), 25029−25036.

(19) Liu, J.; Li, D.; Zhao, W.; Xu, D.; Shi, Z.; Liu, W.; Su, J.; Zhou, T.; Chen, G.; Zhou, D. Excellent Energy Storage Performance Achieved in $Sr(Sc_{0.5}Nb_{0.5})O_3$-Doped $Bi_{0.5}Na_{0.5}TiO_3$-Based Lead-Free Relaxor Ferroelectric Ceramics. *ACS Appl. Energy Mater.* **2024**, *7* (5), 2030−2038.

(20) Balmuchu, S. P.; Malapati, V.; Chilaka, R. R.; Dobbidi, P. Effective Strategy for Achieving Superior Energy Storage Performance in Lead-Free $BaTiO_3$−$Bi(Zn_{2/3}(Nb_{0.85}Ta_{0.15})_{1/3})O_3$ Ferroelectric Ceramics. *Ceram. Int.* **2024**, *50* (8), 13782−13793.

(21) Adediji, Y. B.; Adeyinka, A. M.; Yahya, D. I.; Mbelu, O. V. A Review of Energy Storage Applications of Lead-Free $BaTiO_3$-Based Dielectric Ceramic Capacitors. *Energy, Ecol. Environ.* **2023**, *8*, 401−419.

(22) Lu, D. Y.; Sun, X. Y.; Liu, B.; Zhang, J. L.; Ogata, T. Structural and Dielectric Properties, Electron Paramagnetic Resonance, and Defect Chemistry of Pr-Doped $BaTiO_3$ Ceramics. *J. Alloys Compd.* **2014**, *615*, 25−34.

(23) Dubey, K.; Dubey, S.; Sahu, V.; Parry, R. A.; Modi, A.; Gaur, N. K. Structural, Optical and Magnetic Properties of CoFe2O4 Nanoparticle Synthesized by Ultrasonication-Assisted Sol-Gel Technique. *Appl. Phys. A Mater. Sci. Process.* **2022**, *128* (7), 1−11.

(24) Mesrar, M.; Elbasset, A.; Echatoui, N. S.; Abdi, F.; Lamcharfi, T. D. Studies of Structural, Dielectric, and Impedance Spectroscopy of KBT-Modified Sodium Bismuth Titanate Lead-Free Ceramics. *ACS Omega* **2022**, *7* (42), 37142−37163.

(25) Sati, A.; Pokhriyal, P.; Kumar, A.; Anwar, S.; Sagdeo, A.; Lalla, N. P.; Sagdeo, P. R. Origin of Ferroelectricity in Cubic Phase of Hf Substituted BaTiO3. *J. Phys.: Condens. Matter* **2021**, *33* (16), 165403.

(26) Lu, D. Y.; Sun, X. Y.; Toda, M. A Novel High-k "Y5V" Barium Titanate Ceramics Co-Doped with Lanthanum and Cerium. *J. Phys. Chem. Solids* **2007**, *68* (4), 650−664.

(27) Veerapandiyan, V. K.; Khosravi H, S.; Canu, G.; Feteira, A.; Buscaglia, V.; Reichmann, K.; Deluca, M. B-Site Vacancy Induced Raman Scattering in $BaTiO_3$-Based Ferroelectric Ceramics. *J. Eur. Ceram. Soc.* **2020**, *40* (13), 4684−4688.

(28) Khedhri, M. H.; Abdelmoula, N.; Khemakhem, H.; Douali, R.; Dubois, F. Structural, Spectroscopic and Dielectric Properties of Ca-Doped $BaTiO_3$. *Appl. Phys. A Mater. Sci. Process.* **2019**, *125* (3), 1−13.

(29) Dobal, P. S.; Dixit, A.; Katiyar, R. S.; Yu, Z.; Guo, R.; Bhalla, A. S. Micro-Raman Scattering and Dielectric Investigations of Phase Transition Behavior in the $BaTiO_3$-$BaZrO_3$ System. *J. Appl. Phys.* **2001**, *89* (12), 8085−8091.

(30) Zhou, C.; Feteira, A. Observation of Multiple Dielectric Relaxations in $BaTiO_3$-$Bi(Li_{1/3}Ti_{2/3})O_3$ Ceramics. *Appl. Phys. A Mater. Sci. Process.* **2017**, *123* (11), 1−7.

(31) Pokorńy, J.; Pasha, U. M.; Ben, L.; Thakur, O. P.; Sinclair, D. C.; Reaney, I. M. Use of Raman Spectroscopy to Determine the Site Occupancy of Dopants in BaTiO3. *J. Appl. Phys.* **2011**, *109* (11), 114110.

https://doi.org/10.1021/acsomega.5c04164
ACS Omega 2025, 10, 43779−43796

(32) Sati, A.; Mishra, V.; Kumar, A.; Warshi, M. K.; Sagdeo, A.; Kumar, R.; Sagdeo, P. R. Effect of Structural Disorder on the Electronic and Phononic Properties of Hf Doped BaTiO 3. *J. Mater. Sci. Mater. Electron.* **2019**, *30* (10), 9498−9506.
(33) Zhang, J.; Hao, H.; Guo, Q.; Yao, Z.; Cao, M.; Liu, H. Dielectric and Anti-Reduction Properties of $BaTiO_3$-Based Ceramics for MLCC Application. *Ceram. Int.* **2023**, *49* (15), 24941−24947.
(34) Shi, J.; Zhao, Y.; He, J.; Li, T.; Zhu, F.; Tian, W.; Liu, X. Deferred Polarization Saturation Boosting Superior Energy-Storage Efficiency and Density Simultaneously under Moderate Electric Field in Relaxor Ferroelectrics. *ACS Appl. Energy Mater.* **2022**, *5* (3), 3436−3446.
(35) Hossain, M. S.; Das, S. K.; Moniruzzaman, M.; Hakim, M. A.; Basith, M. A. Frequency and Temperature Dependent Electric Polarization, Relaxation, and Transport Properties of Mo and W Doped $BaTiO_3$. *Results Phys.* **2021**, *30*, No. 104873.
(36) Liu, X.; Huang, Q.; Peng, Y.; Guan, Y.; Du, Y.; Mao, H.; Lv, J. Phase-Field Simulation and Experimental Validation of Mo-Doping Effects on NbC−Ni Cermets during Liquid Phase Sintering. *J. Am. Ceram. Soc.* **2025**, *108*, No. e70075.
(37) Utt, D.; Stukowski, A.; Albe, K. Grain Boundary Structure and Mobility in High-Entropy Alloys: A Comparative Molecular Dynamics Study on a Σ11 Symmetrical Tilt Grain Boundary in Face-Centered Cubic CuNiCoFe. *Acta Mater.* **2020**, *186*, 11−19.
(38) Tanahashi, M.; Ito, M.; Murao, M.; Iga, A. Effect of Al-Doping on the Grain Growth of ZnO. *Jpn. J. Appl. Phys.* **1997**, *36*, L573−L576.
(39) Siemek, K.; Olejniczak, A.; Korotkov, L. N.; Konieczny, P.; Belushkin, A. V. Investigation of Surface Defects in BaTiO3 Nanopowders Studied by XPS and Positron Annihilation Lifetime Spectroscopy. *Appl. Surf. Sci.* **2022**, *578*, No. 151807.
(40) Siril, V. S.; Ihsan Ali, P. V.; Madhusoodanan, K. N. Sol-Gel Synthesis and Investigation of Dielectric Behaviour in Barium Stannate. *Mater. Today Proc.* **2022**, *62*, 530−534.
(41) Xie, P.; Yang, F.; Li, R.; Ai, C.; Lin, C.; Lin, S. Improving Hydrogen Evolution Activity of Perovskite BaTiO3 with Mo Doping: Experiments and First-Principles Analysis. *Int. J. Hydrogen Energy* **2019**, *44* (23), 11695−11704.
(42) Srisombat, L.; Ananta, S.; Singhana, B.; Lee, T. R.; Yimnirun, R. Chemical Investigation of Fe3+/Nb5+-Doped Barium Titanate Ceramics. *Ceram. Int.* **2013**, *39*, S591.
(43) Lin, H. Y.; Shih, C. Y. Efficient One-Pot Microwave-Assisted Hydrothermal Synthesis of M (M = Cr, Ni, Cu, Nb) and Nitrogen Co-Doped TiO_2 for Hydrogen Production by Photocatalytic Water Splitting. *J. Mol. Catal. A Chem.* **2016**, *411*, 128−137.
(44) Ji, R.; Cheng, J.; Yang, X.; Yu, J.; Li, L. Enhanced Charge Carrier Transport in Spray-Cast Organic Solar Cells Using Solution Processed MoO_3 Micro Arrays. *RSC Adv.* **2017**, *7* (6), 3059−3065.
(45) Tran, H. N.; Park, S.; Wibowo, F. T. A.; Krishna, N. V.; Kang, J. H.; Seo, J. H.; Nguyen-Phu, H.; Jang, S. Y.; Cho, S. 17% Non-Fullerene Organic Solar Cells with Annealing-Free Aqueous MoOx. *Adv. Sci.* **2020**, *7* (21), No. 2002395.
(46) Song, H.; Kim, Y. T. A Mo-Doped $TiNb_2O_7$ Anode for Lithium-Ion Batteries with High Rate Capability Due to Charge Redistribution. *Chem. Commun.* **2015**, *51* (48), 9849−9852.
(47) Prajapati, K.; Singh, A. K. Improved Ferroelectric and Piezoelectric Properties and Structural Correlations in a New Ceramic $0.38Ba(Cu_{1/3}Nb_{2/3})O_3$−$0.62PbTiO_3$ by MnO2 Additive. *J. Mater. Res.* **2023**, *38* (8), 2031−2048.
(48) Frankcombe, T. J.; Liu, Y. Interpretation of Oxygen 1s X-Ray Photoelectron Spectroscopy of ZnO. *Chem. Mater.* **2023**, *35* (14), 5468−5474.
(49) Sun, W.; Liu, J.; Ran, F.; Li, N.; Li, Z.; Li, Y.; Wang, K. Step-Scheme CsPbBr 3/BiOBr Photocatalyst with Oxygen Vacancies for Efficient CO2 Photoreduction. *Dalt. Trans.* **2024**, *53* (33), 14018−14027.
(50) Mala, D.; Singh, C. B.; Singh, A. K. Synthesis and Characterization of $BaTi_{1-x}Nb_xO_3$ Ferroelectric Perovskite Oxides with Tunable Band Gap, Anomalous Photovoltage, and Enhanced Energy Storage. *J. Mater. Sci. Mater. Electron.* **2024**, *35* (13), 1−15.
(51) Mühlenbein, L.; Singh, C. B.; Singh, A. K.; Fina, I.; Himcinschi, C.; Lotnyk, A.; Bhatnagar, A. Control of Layering in Aurivillius Phase Nanocomposite Thin Films and Influence on Ferromagnetism and Optical Absorption. *ACS Appl. Electron. Mater.* **2022**, *4* (4), 1997−2004.
(52) Singh, V. P.; Satyarthi, S. K.; Dwivedi, A.; Dwivedi, A.; Singh, A. K. Boosting Energy Storage of Poly(Vinylidene Difluoride) Nanocomposite Based Flexible Self-Standing Film with Low Amount of Hydroxylated V_2O_5. *ACS Appl. Energy Mater.* **2022**, *5* (10), 12837−12850.
(53) Bhal Singh, C.; Kumar Verma, N.; Kumar Singh, A. Synthesis and Band-Gap Tuning of (Co, Bi) Doped $PbTiO_3$ for Photoferroelectrics Applications. *Integr. Ferroelectr.* **2018**, *194* (1), 145−151.
(54) Singh, C. B.; Singh, A. K.; Verma, N. K. Development of Low Band Gap Layered $Bi_6FeNiTi_3O_{18}$ Aurivillius Phase Ceramics for Ferroelectric Memory and Cathode for Lithium-Oxygen Batteries Applications. *J. Mater. Sci. Mater. Electron.* **2024**, *35* (6), 1−14.
(55) Gou, G. Y.; Bennett, J. W.; Takenaka, H.; Rappe, A. M. Post Density Functional Theoretical Studies of Highly Polar Semiconductive Pb(Ti1-XNix)O3−x Solid Solutions: Effects of Cation Arrangement on Band Gap. *Phys. Rev. B - Condens. Matter Mater. Phys.* **2011**, *83* (20), 1−7.
(56) Zhang, Y.; Zhang, G.; Li, A.; Zhang, J.; Zheng, Y.; Luo, G.; Tu, R.; Zhang, J.; Shen, Q.; Zhang, L. Enhancement of Energy Storage Performance in Lead-Free Relaxor Ferroelectric Ceramics via Band Structure Engineering. *Am. Ceram. Soc.* **2023**, *106*, 6630−6640.
(57) Patil, D. R.; Lokare, S. A.; Devan, R. S.; Chougule, S. S.; Kanamadi, C. M.; Kolekar, Y. D.; Chougule, B. K. Studies on Electrical and Dielectric Properties of $Ba_{1-x}Sr_x$ TiO_3. *Mater. Chem. Phys.* **2007**, *104*, 254−257.
(58) Saikia, K. K.; Haque, S. U.; Murugesan, G.; Kalainathan, S. Dielectric Relaxation in CoFe2−xYxO4 (x = 0.2, 0.4, 0.6) Prepared by Hydrothermal Method. *J. Mater. Sci.: Mater. Electron.* **2017**, *28*, 6583−6591.
(59) Dutta, S.; Ali, M. S.; Tama, A. M.; Parvez, M. M.; Ferdous, H.; Hakim, M. A.; Hossain, M. S. Enhancement of Dielectric Properties and Conduction Mechanism in $BaTi_{0.85}Sn_{0.15}O_3$ for Energy Storage Application. *J. Energy Storage* **2023**, *72*, No. 109335.
(60) Hossain, M. S.; Das, S. K.; Moniruzzaman, M.; Hakim, M. A.; Basith, M. A. Results in Physics Frequency and Temperature Dependent Electric Polarization, Relaxation, and Transport Properties of Mo and W Doped BaTiO 3. *Results Phys.* **2021**, *30*, No. 104873.
(61) Kushvaha, D. K.; Rout, S. K.; Tiwari, B. Physica B: Physics of Condensed Matter Significant Modulation in Field-Induced Energy Storage Capability of BNKT-BN Ceramics. *Phys. B Phys. Condens. Matter* **2022**, *640* (May), No. 414030.
(62) Wang, H.; Bu, X.; Zhang, X.; Zheng, P.; Li, L.; Wen, F.; Bai, W.; Zhang, J.; Zheng, L.; Zhang, Y. Pb/Bi-Free Tungsten Bronze-Based Relaxor Ferroelectric Ceramics with Remarkable Energy Storage Performance. *ACS Appl. Energy Mater.* **2021**, *4*, 9066.
(63) Zhu, C.; Ye, W.; Zheng, P.; Zhang, H.; Lu, F.; Fan, Q.; Zhang, J.; Zheng, L.; Zhang, Y.; Bai, W. Fantastic Energy Storage Performances and Excellent Stability in $BiFeO_3$−$SrTiO_3$-Based Relaxor Ferroelectric Ceramics. *ACS Appl. Energy Mater.* **2022**, *5*, 8492−8500.
(64) Luo, G.; Li, A.; Zhang, Y.; Zhang, G.; Sun, Y.; Tu, R.; Shen, Q. Improvement of Energy Storage Properties of $NaNbO_3$ -Based Ceramics through the Cooperation of Relaxation and Oxygen Vacancy Defects. *Ceram. Int.* **2023**, *49*, 801−807.
(65) Peng, Z.; Wang, J.; Niu, M.; Nie, X.; Xu, S.; Zhang, F.; Wang, J.; Wu, D.; Yang, Z.; Chao, X. Structure, Electrical Properties and Energy Storage Performance of BNKT-BMN Ceramics. *J. Mater. Sci.: Mater. Electron.* **2022**, *33*, 3053−3064.
(66) Reda, M.; El-Dek, S. I.; Arman, M. M. Improvement of Ferroelectric Properties via Zr Doping in Barium Titanate Nanoparticles. *J. Mater. Sci. Mater. Electron.* **2022**, *33* (21), 16753−16776.

https://doi.org/10.1021/acsomega.5c04164
ACS Omega 2025, 10, 43779−43796

(67) Luo, N.; Hu, C.; Han, K.; Liu, L.; Peng, B.; Wang, X.; Zhou, H.; Feng, Q.; Chen, X.; Wei, Y. Lead - Free $Ag_{1-3x}La_xNbO_3$ Antiferroelectric Ceramics with High - Energy Storage Density and Efficiency. *Am. Ceram. Soc.* **2019**, *102*, 4640−4647.
(68) Chakchouk, N.; Karoui, K.; Drissi, N.; Jomni, F.; Rhaiem, A. B. An Investigation of Structural, Thermal, and Electrical Conductivity Properties for Understanding Transport Mechanisms of $CuWO_4$ and a-$CuMoO_4$ Compounds. *RSC Adv.* **2024**, *14*, 46−58.
(69) Zhou, M.; Liang, R.; Zhou, Z.; Dong, X. Combining High Energy Efficiency and Fast Charge-Discharge Capability in Novel $BaTiO_3$-Based Relaxor Ferroelectric Ceramic for Energy-Storage. *Ceram. Int.* **2019**, *45* (3), 3582−3590.
(70) Zahn, M.; Müller, A. M.; Kelley, K. P.; Neumayer, S.; Kalinin, S. V.; Kézsmarki, I.; Fiebig, M.; Lottermoser, T.; Domingo, N.; Meier, D.; Schultheiß, J. Reversible Long-Range Domain Wall Motion in an Improper Ferroelectric. *Nat. Commun.* **2025**, *16*, 1781.
(71) Jin, L.; Li, F.; Zhang, S. Decoding the Fingerprint of Ferroelectric Loops: Comprehension of the Material Properties and Structures. *J. Am. Ceram. Soc.* **2014**, *97* (1), 1−27.
(72) Ghayour, H.; Abdellahi, M. A Brief Review of the Effect of Grain Size Variation on the Electrical Properties of $BaTiO_3$-Based Ceramics. *Powder Technol.* **2016**, *292*, 84−93.
(73) Kumar, A.; Lee, G.; Chae, Y. G.; Thakre, A.; Choi, H. S.; Nam, G. H.; Ryu, J. Induced Slim Ferroelectric Hysteresis Loops and Enhanced Energy-Storage Properties of Mn-Doped (Pb0·93La0.07)(Zr0·82Ti0.18)O3 Anti-Ferroelectric Thick Films by Aerosol Deposition. *Ceram. Int.* **2021**, *47* (22), 31590−31596.
(74) Huang, C. J.; Li, K.; Wu, S. Y.; Zhu, X. L.; Chen, X. M. Variation of Ferroelectric Hysteresis Loop with Temperature in $(Sr_xBa_{1-x})Nb_2O_6$ Unfilled Tungsten Bronze Ceramics. *J. Mater.* **2015**, *1* (2), 146−152.

https://doi.org/10.1021/acsomega.5c04164
ACS Omega 2025, 10, 43779−43796